IEEE Journal of Translational Engineering in Health and Medicine

Received 28 August 2016; revised 1 December 2016; accepted 10 January 2017.
Date of publication 23 February 2017; date of current version 28 March 2017.

Digital Object Identifier 10.1109/JTEHM.2017.2665496

Spatiotemporal Strategies for Joint Segmentation and Motion Tracking From Cardiac Image Sequences

HUAFENG LIU[1], TING WANG[1], LEI XU[2], AND PENGCHENG SHI[3]

[1]State Key Laboratory of Modern Optical Instrumentation, Zhejiang University, Hangzhou 310027, China
[2]Department of Radiology, Beijing Anzhen Hospital, Capital Medical University, Beijing 100029, China
[3]B. Thomas Golisano College of Computing and Information Sciences, Rochester Institute of Technology, Rochester, NY 14623, USA

CORRESPONDING AUTHOR: H. LIU (liuhf@zju.edu.cn)

This work was supported in part by the National Natural Science Foundation of China under Grant 61525106 and Grant 61427807, in part by the National Key Technology Research and Development Program of China under Grant 2016YFC1300302, in part by the Shenzhen Innovation Funding under Grant SGLH20131010110119871 and Grant GJHZ20140415152115754, and in part by the Zhejiang Province Science and Technology Projects under Grant 2015C33061.

ABSTRACT Although accurate and robust estimations of the deforming cardiac geometry and kinematics from cine tomographic medical image sequences remain a technical challenge, they have significant clinical value. Traditionally, boundary or volumetric segmentation and motion estimation problems are considered as two sequential steps, even though the order of these processes can be different. In this paper, we present an integrated, spatiotemporal strategy for the simultaneous joint recovery of these two ill-posed problems. We use a mesh-free Galerkin formulation as the representation and computation platform, and adopt iterative procedures to solve the governing equations. Specifically, for each nodal point, the external driving forces are individually constructed through the integration of data-driven edginess measures, prior spatial distributions of myocardial tissues, temporal coherence of image-derived salient features, imaging/image-derived Eulerian velocity information, and cyclic motion model of myocardial behavior. The proposed strategy is accurate and very promising application results are shown from synthetic data, magnetic resonance (MR) phase contrast, tagging image sequences, and gradient echo cine MR image sequences.

INDEX TERMS Mesh-free, segmentation, cardiac motion tracking, joint estimation.

I. INTRODUCTION

Because coronary heart diseases often manifest as abnormalities of the ventricular geometry and wall kinematics, noninvasive cine medical imaging techniques are of significant clinical value, such as magnetic resonance imaging (MRI), to provide shape and motion information of the myocardium ([1]–[4]). In the past three decades, there has been a large increase in the number of cardiac image analysis methods to assess the shape and motion parameters from image sequences that describe the functionality of the heart. However, several challenges remain.

As the first step for motion tracking, registration, and many other cardiac imaging analyses, segmentation is often needed to isolate the myocardium from the background information throughout the cardiac cycle before further processing. The difficulties of this process arise from the presence of noise, lack of edge information for the epicardium, and intensity inhomogeneities. Accordingly, many approaches have been developed for myocardial contour delineation to overcome these issues, including the use of dynamic programming ([5]), probability atlas ([6]), active shape model (ASM) ([7], [8]), active appearance model (AAM) ([9], [10]), combination of ASM and AAM ([11]), constrained pattern matching strategy ([12]), proactive deformable model ([13]), and motion-guided segmentation framework ([14], [15]). In addition to the continuing progress in cardiac image segmentation, considerable efforts have also been focused on motion and deformation recovery from image sequences. Imaging-derived kinematic constraints, such as salient point correspondence and Eulerian velocity, provide the initial estimates of the myocardium. Various regularization strategies, including

mathematical smoothness ([16]–[19]), continuum mechanics models ([20]), and electromechanical models ([13], [21]), are adopted to constrain the ill-posed problem for recovering the dense field motion and deformation parameters of the heart. In addition, several attempts have been made to track the motion over the entire cardiac cycle by using the explicit temporal modeling of cyclic heart dynamics, from forward and backward Kalman filters ([22], [23]) to Fourier harmonics tracking ([24]).

Thus far, most existing efforts have not attempted to tackle segmentation and motion problems in a joint or simultaneous fashion; rather, these have been treated as two sequential processes. Obviously, cardiac segmentation and motion tracking problems are closely related, and the robustness and effectiveness of these methods can be enhanced significantly by coupling them. In other applications, it has been shown that treating the spatial boundary finding and spatiotemporal motion tracking problems as a coherent and unified process can achieve more consistent and probably more approximate results ([25]–[27]). In this manner, we can use the total available information provided by the image sequence in a more complete manner, and reduce the possibility of error propagation from one step to another to achieve potentially more robust analysis results.

In this paper, a unified framework is presented that simultaneously recovers the boundary shape and motion information of the heart over the entire image sequence. Our effort adopts the energy minimization formulation of deformable models through the integration of various data-driven image constraints and intrinsic model constraints that guide the spatiotemporal model evolution process. Specifically, gradient measures and gradient vector fields ([28]) provide edginess information; image-derived geometrical tokens, i.e., the isointensity curvature, are used to establish the likelihood measure for shape-based correspondence matching; frame-to-frame Eulerian velocity fields, i.e., MR phase contrast images and optical flow maps, bias the direction and magnitude of the model movement; and the physical model regularizes the behavior between neighboring points. Furthermore, a temporally cyclical model of the cardiac boundary motion is incorporated to reduce the feasible space of the moving contour. To achieve segmentation and motion recovery simultaneously, we use iterative procedures to evolve the heart tissue under the external image derived and prior model based driving forces. The work reported here provides a detailed description of our earlier effort ([29]) with careful validation based on synthetic data, animal models, and human MR image sequences.

We realize that several efforts are of relevance to our work ([30], [31]). An incompressible-model-based registration method for cardiac deformation recovery from cine MRI has been proposed ([32]). A generalized robust point matching strategy with a boundary element method was used for the recursive recovery of shape and motion through a cardiac image sequence. Our work is different in that it is constrained by biomechanically motivated system dynamics, and it is implemented in a mesh-free framework to overcome finite element method (FEM) limitations.

II. METHODOLOGY

Our strategy is based on a physically motivated active region model in which each node spatiotemporally evolves under the influences of the node-dependent imaging data, temporal consistency models of the tissue geometry and kinematics, and statistical priors of the myocardium spatial distributions. First the approach is formulated as an energy minimization problem for each image frame, then we use the mesh-free representation and iterative procedures to solve it.

A. OVERVIEW OF FRAMEWORK

Under the influence of the image data and prior model constraints, the heart behaves as an elastic object, which has three integral components: (1) a topological and geometric representation of the object, which is presented in section II-B; (2) a material constitutive law that defines the intrinsic dynamic behavior of the object, which is discussed in detail in section II-C; and (3) the external driving forces that move and deform the object toward equilibrium, which is discussed in section II-D.

The unified segmentation and motion analysis framework is posed as an energy minimization problem:

$$\hat{u} = \arg\min_{u} \int_{\Omega} \left(E_{internal}(u) + E_{external}(u)\right) d\Omega \qquad (1)$$

where:

- u is the displacement field defined over the region of interest Ω;
- the internal energy function $E_{internal}$ imposes regularity constraints on the solution, and it is solely defined by the object's deformation and intrinsic material properties; and
- the external energy $E_{external}$ includes both segmentation cues and motion tracking terms needed to deform the current object configuration towards the new equilibrium state.

Using Galerkin's principles, energy functionals are formulated in terms of the nodal displacements $\mathbf{U}$, and we can express the resulting set of differential governing equations in matrix form as

$$K\mathbf{U} = F \qquad (2)$$

where K is the assembled global stiffness matrix which describes the material elasticity of the object, and F is the external driving force that tries to deform the object to adhere to the image data and prior information. We can interpret this equation as the model spatiotemporally evolving toward the equilibrium state under the internal spatial constraints of K, which provides the relationship between nodes and the space-time dependent external forces F. By taking finite differences in the time domain, with time step τ, we use an explicit Euler time integration procedure to integrate equation (2) through

IEEE Journal of Translational Engineering in Health and Medicine

time. Specifically, the Lagrangian evolution can be presented as

$$(I + \tau K)\mathbf{U}^t = (\mathbf{U}^{t-1} + \tau F^{t-1}) \tag{3}$$

therefore,

$$\mathbf{U}^t = (I + \tau K)^{-1}(\mathbf{U}^{t-1} + \tau F^{t-1}) \tag{4}$$

where I is an identity matrix, $\mathbf{U}^t$ and $\mathbf{U}^{t-1}$ are the displacement at step t and $t-1$, respectively, and F^{t-1} is the force vector at step $t-1$. The evolution is stopped when the external force F diminishes and/or when the displacement difference between iterations $\|\mathbf{U}^t - \mathbf{U}^{t-1}\|$ is below a certain threshold.

B. GEOMETRICAL REPRESENTATION

How to represent the heart structures in a computational environment is an important issue, because this affects the numerical accuracy, computational feasibility, and implementation difficulty. FEM has been widely used in computational cardiology, but for cardiac image analysis, it's probably not the best choice. We adopt mesh-free methods in our framework. By using the mesh-free methods, the heart is represented by a set of nodes bounded by surfaces which represents the heart boundaries. As no meshing is involved, the distribution of nodes is more flexible, thus facilitating adaptive refinements to improve the regional numerical accuracy. Furthermore, the intrinsic h-p (spatial refinements and orders of polynomial) adaptivity of the mesh-free methods facilitates the incorporation of high-order polynomials, and thus, the number of nodes required is smaller than that of linear FEM for the same accuracy.

1) FEM VS. MESH-FREE

To obtain a continuous cardiac motion field from a sparse set of data efficiently and accurately, a proper representation and computation strategy for the myocardium is necessary. For the last few decades, FEM has been widely used for motion field approximations in cardiac analysis because of its effectiveness and general applicability. With FEM, the complicated continuous solution domain is discretized into much simpler sub-domains (elements) with known polynomials, such as triangles in 2D and tetrahedra in 3D, to provide relationships with the sampling nodes. With such discretizations, the complicated physical and mathematical models can be approximated and solved by sets of governing algebraic equations.

However, there are some inherent limitations in the FEM representation of the myocardium. First, the FEM result is highly related to the number of finite element meshes. In practice, because of the heart's motion nature, some elements of the mesh will become compressed or even skewed. This problem could be solved by mesh refinements and remeshing; however, the procedures are very computationally expensive, especially in 3D cases. More crucially, it is difficult to handle fiber orientation discontinuities in the FEM representation. The mesh-free representation has the potential to overcome these drawbacks, in which the geometry of the heart is represented by unstructured, adaptively sampled nodes that are bounded by the boundaries of the object. As no mesh is required, the density of the nodes can be refined adaptively by simply adding or removing nodes in the problem domain, depending on the available computational resources and required preciseness. Furthermore, it has been shown that the mesh-free method better handles the fiber orientations and kinematics/material discontinuities, and it also has better h-p adaptivity.

In this paper, the mesh-free representation of the myocardium is used. Typically, ECG-gated MRI image sequences are acquired over the heart cycle, which are in 16–20 frames consisting of 10–16 slices each. The endocardial and epicardial boundaries of the cardiac image in the first frame are segmented using the existing level set framework ([33]). We generate intermediate contours at the desired distance by interpolating between contours. The endocardial and epicardial surfaces are then reconstructed using Delaunay triangulation and are smoothed using the non-shrinking algorithm. The myocardial sample points together with the endocardial and epicardial surfaces or boundaries of a selected mid-ventricular slice in 2D form the mesh-less representation of the heart. Specifically, we can attach the local fiber orientation to each sampling node depending on its location, thus the fiber structure can be represented efficiently.

In the mesh-free representation of the heart, the nodes can have adaptive and non-uniform distributions over time and space, and are more densely distributed in areas with large shape variation and large displacement gradient, and the initial distribution quality should not be mainly concerned.

2) MESH-FREE REPRESENTATION OF THE MYOCARDIUM

a: SHAPE FUNCTION CONSTRUCTION: MLS

By using the finite element formulation, we use an isoparametric formulation defined in a natural coordinate system, in which the same basis functions are used in the interpolations of the element coordinates and the element displacements. For the mesh-free particle representation, shape functions need to be created to approximate the field function by using their values at sampling nodes in the analysis domain. In particular, the shape functions are constructed by using the moving least squares (MLS) approximation.

Let $u(\mathbf{x})$ be the displacement field defined in the myocardial domain Ω, and $u^h(\mathbf{x})$ be the approximation of $u(\mathbf{x})$ at point $\mathbf{x}$ as given by the MLS approximation:

$$u^h(\mathbf{x}) = \sum_{j=1}^{m} p_j(\mathbf{x})a_j(\mathbf{x}) \equiv \mathbf{p}^T(\mathbf{x})\mathbf{a}(\mathbf{x}) \tag{5}$$

where $\mathbf{p}(\mathbf{x})$ is the polynomial basis function, m is the number of terms of monomials (polynomial basis), and $\mathbf{a}(\mathbf{x})$ is a vector of unknown location-dependent coefficients. Given a set of n nodal values at nodes $x_1, x_2, \ldots, x_n$ that are in the influence domain, $\mathbf{a}(\mathbf{x})$ can be obtained at any point $\mathbf{x}$ by minimizing a

weighted, discrete L_2 norm:

$$J = \sum_{i=1}^{n} w(\mathbf{x} - \mathbf{x}_i)[\mathbf{p}^T(\mathbf{x}_i)\mathbf{a}(\mathbf{x}) - u_i]^2 \tag{6}$$

where n is the number of node points $\mathbf{x}_i$ in the neighborhood of $\mathbf{x}$ (*influence domain*) for which the weight function is $w(\mathbf{x}-\mathbf{x}_i) \neq 0$, and the nodal value is $u_i = u(\mathbf{x}_i)$. The shape of the influence domain of x can be square or circular. We use square domain in this paper.

The stationarity of J in Equation (6) with respect to $\mathbf{a}(\mathbf{x})$, $\frac{\partial J}{\partial \mathbf{a}} = 0$, leads to

$$\mathbf{a}(\mathbf{x}) = \mathbf{A}^{-1}(\mathbf{x})\mathbf{B}(\mathbf{x})\mathbf{U} \tag{7}$$

where

$$\mathbf{A}(\mathbf{x}) = \sum_{i=1}^{n} w(\mathbf{x} - \mathbf{x}_i)\mathbf{p}(\mathbf{x}_i)\mathbf{p}^T(\mathbf{x}_i) \tag{8}$$

$$\mathbf{B}(\mathbf{x}) = [\mathbf{B_1}, \mathbf{B_2}, \ldots, \mathbf{B_n}] \tag{9}$$

with $\mathbf{B}_i = w(\mathbf{x} - \mathbf{x}_i)\mathbf{p}(\mathbf{x}_i)$ and $\mathbf{U}^T = \{u_1, u_2, ..., u_n\}$. Note that we require $n \gg m$, which prevents the singularity of the matrix $\mathbf{A}(\mathbf{x})$ and ensures the existence of $\mathbf{A}^{-1}(\mathbf{x})$, and this condition can be guaranteed by the size of the adaptively controlled influence domain. Substituting the results into Equation (5) gives

$$u^h(\mathbf{x}) = \sum_{i=1}^{n}\sum_{j=1}^{m} p_j(\mathbf{x})(\mathbf{A}^{-1}(\mathbf{x})\mathbf{B}(\mathbf{x}))_{ji}u_i \tag{10}$$

The above equation can also be written in matrix form:

$$u^h(\mathbf{x}) = \mathbf{N}(\mathbf{x})\mathbf{U} \tag{11}$$

where the MLS-derived shape function $\mathbf{N}(\mathbf{x})$ is defined by

$$\mathbf{N}(\mathbf{x}) = \mathbf{p}^T(\mathbf{x})\mathbf{A}^{-1}(\mathbf{x})\mathbf{B}(\mathbf{x}) \tag{12}$$

and $\mathbf{N}(\mathbf{x}) = [N_1(\mathbf{x}), N_2(\mathbf{x}), ..., N_n(\mathbf{x})]$ corresponding to n nodes in the domain.

To determine the spatial derivatives of the field variable's function, obtaining the derivatives of the *MLS* shape functions is necessary. For convenience, we set

$$r(\mathbf{x}) = \mathbf{A}(\mathbf{x})^{-1}\mathbf{p}(\mathbf{x}) \tag{13}$$

then

$$\mathbf{N}(\mathbf{x}) = r^T(\mathbf{x})\mathbf{B}(\mathbf{x}) \tag{14}$$

Thus, we can obtain the partial derivatives of the shape function $\mathbf{N}$ from the partial derivatives of $r(\mathbf{x})$ as follows:

$$\mathbf{N}_{,i_x}(\mathbf{x}) = r_{,i_x}(\mathbf{x})\mathbf{B}(\mathbf{x}) + r(\mathbf{x})\mathbf{B}_{,i_x}(\mathbf{x}) \tag{15}$$

$$\mathbf{N}_{,i_x i_y} = r_{,i_x i_y}\mathbf{B} + r_{,i_x}\mathbf{B}_{,i_y} + r_{,i_y}\mathbf{B}_{,i_x} + r\mathbf{B}_{,i_x i_y} \tag{16}$$

$$\begin{aligned}\mathbf{N}_{,i_x i_y i_z} = {} & r_{,i_x i_y i_z}\mathbf{B} + r_{,i_x i_y}\mathbf{B}_{,i_z} + r_{,i_x i_z}\mathbf{B}_{,i_y} \\ & + r_{,i_y i_z}\mathbf{B}_{,i_x} + r_{,i_x}\mathbf{B}_{,i_y i_z} + r_{,i_y}\mathbf{B}_{,i_x i_z} \\ & + r_{,i_z}\mathbf{B}_{,i_x i_y} + r\mathbf{B}_{,i_x i_y i_z}\end{aligned} \tag{17}$$

where i_x, i_y, and i_z denote the coordinates. A comma designates a partial derivative with respect to the indicated spatial variable.

b: WEIGHT FUNCTION DESCRIPTION

From the above equations, we can see that the weighting function $w(\mathbf{x}-\mathbf{x}_i)$ is important in determining $\mathbf{A}(\mathbf{x})$ and $\mathbf{B}(\mathbf{x})$. This weighting function should be positive (ensure a meaningful presentation of the physical phenomena) and compact (smooth and continuous over the entire domain). The continuous approximation of the shape function can be achieved by choosing appropriate weighting functions instead of using a high-order basis $\mathbf{p}(\mathbf{x})$, which is an attractive property of the MLS approximation. In 2D space:

$$\mathbf{p}^T(\mathbf{x}) = \{1, x, y, xy, x^2, y^2, \ldots, x^m, y^m\} \tag{18}$$

In 3D space:

$$\mathbf{p}^T(\mathbf{x}) = \{1, x, y, z, xy, yz, zx, x^2, y^2, z^2, \ldots, x^m, y^m, z^m\} \tag{19}$$

where m has the same meaning as in equation (5).

Let $\bar{r} = |\mathbf{x} - \mathbf{x}_I|/d_{mI}$. Then, the weight function is given by

$$w(\mathbf{x} - \mathbf{x}_i) = w(\bar{r}) = \begin{cases} \frac{2}{3} - 4\bar{r}^2 + 4\bar{r}^3 & \text{for } \bar{r} \leq \frac{1}{2} \\ \frac{4}{3} - 4\bar{r} + 4\bar{r}^2 - \frac{4}{3}\bar{r}^3 & \text{for } \frac{1}{2} < \bar{r} \leq 1 \\ 0 & \text{for } \bar{r} > 1 \end{cases} \tag{20}$$

The support size d_{mI} of the I^{th} node is determined by $d_{mI} = d_{max}c_I$, where d_{max} is a scaling parameter, and the distance c_I is determined by searching for enough neighbor nodes to ensure the singularity of the matrix $\mathbf{A}$ in Equation (8).

C. INTRINSIC MATERIAL CONSTRAINTS

To regularize our region model's intrinsic behavior, physically more meaningful continuum mechanics models are adopted. Although models of different complexities are available, as our goal is to study the subject-specific cardiac physiology through medical images, the models chosen should be detailed enough to include macroscopic cardiac properties such as fiber orientations and anisotropic material properties; however, they should not be too complicated such that many parameters cannot be determined using the available knowledge or measurements. Consequently, a biomechanical model has been used.

1) BIOMECHANICAL MODEL OF THE MYOCARDIUM

The mechanical model can be defined in terms of an internal energy function that describes the state of the material.

In our 2D implementation, we can model the myocardium as an isotropic linear elastic material, which provides a reasonable framework to aid the recovery of shape and motion. Under two dimensional Cartesian coordinate system, this is defined in terms of the linear isotropic constitutive law:

$$\sigma = C\varepsilon \tag{21}$$

where σ is the stress vector and C is the stress-strain or material matrix. Assuming the displacement along the $x-$ and $y-$axis to be $u(x, y)$ and $v(x, y)$ respectively, the infinitesimal strain tensor ε is defined as:

$$\varepsilon = \begin{bmatrix} \frac{\partial u}{\partial x} \\ \frac{\partial v}{\partial y} \\ \frac{\partial u}{\partial y} + \frac{\partial v}{\partial x} \end{bmatrix} = \begin{bmatrix} \partial/\partial x & 0 \\ 0 & \partial/\partial y \\ \partial/\partial y & \partial/\partial x \end{bmatrix} \begin{bmatrix} u \end{bmatrix} = \mathbf{LU} \tag{22}$$

where $\mathbf{L}$ is a differential operator matrix which depends on the strain types (infinitesimal or finite). Under plane strain situations, the material matrix C is:

$$C = \frac{E_y}{(1+\nu)(1-2\nu)} \begin{bmatrix} 1-\nu & \nu & 0 \\ \nu & 1-\nu & 0 \\ 0 & 0 & \frac{1-2\nu}{2} \end{bmatrix} \tag{23}$$

Here, E_y is the Young's modulus that is measure of the stiffness of the material and the Poisson's ratio ν is the measure of incompressibility.

Biomechanics studies have demonstrated that myocytes, which connect to each other by collagen to form fibers, occupy 70% of the ventricular wall volume ([34], [35]). It means that cardiac tissues have different properties along and across fibers ([35]). Thus in three dimensional cases, it is more suitable to use a transversely elastic model to describe the intrinsic behavior of the myocardium. This is an extension of the isotropic linear elastic model which allows for one of the three material axes to have a different stiffness from the other two. For such a material, the stress (σ) and strain (ϵ) constitutive laws still obey Hooke's law in a particular orientation (along or across the myofiber).

Let us define C_0 as the material matrix with 0^o (along x-axis) fiber orientation of a point in the myocardium:

$$C_0 = \begin{bmatrix} \frac{1}{E_f} & -\frac{\upsilon_f}{E_{cf}} & -\frac{\upsilon_f}{E_{cf}} & 0 & 0 & 0 \\ -\frac{\upsilon_f}{E_{cf}} & \frac{1}{E_{cf}} & -\frac{\upsilon_{cf}}{E_{cf}} & 0 & 0 & 0 \\ -\frac{\upsilon_f}{E_{cf}} & -\frac{\upsilon_{cf}}{E_{cf}} & \frac{1}{E_{cf}} & 0 & 0 & 0 \\ 0 & 0 & 0 & \frac{1}{G} & 0 & 0 \\ 0 & 0 & 0 & 0 & \frac{1}{G} & 0 \\ 0 & 0 & 0 & 0 & 0 & \frac{2(1+\upsilon_{cf})}{E_{cf}} \end{bmatrix}^{-1} \tag{24}$$

Here, E_f, E_{cf}, υ_f, and υ_{cf} are the Young's moduli and Poisson's ratios along and cross the fiber, respectively. $G = E_f/(2(1+\upsilon_f))$ describes the shearing property. For isotropic materials, C_0 reduces to the matrix if $E_f = E_{cf}$ and $v_f = v_{cf}$.

Since the fiber orientation varies in different regions of the left ventricle ([34]), assuming that the local coordinate system has θ_h degrees horizontal angle and ϕ_v degrees vertical angle apart from the global coordinate system, the corresponding material matrix at any point can be obtained using the tensor transformation:

$$C = T^{-1} C_0 R T R^{-1} \tag{25}$$

T is a combination transformation matrix of T_{vert} and T_{hori}:

$$T = T_{vert} T_{hori} \tag{26}$$

with (27), (28) as shown at the bottom of this page:

Matrix R represents the transformation between strain and engineering strain:

$$R = \begin{bmatrix} 1 & 0 & 0 & 0 & 0 & 0 \\ 0 & 1 & 0 & 0 & 0 & 0 \\ 0 & 0 & 1 & 0 & 0 & 0 \\ 0 & 0 & 0 & 2 & 0 & 0 \\ 0 & 0 & 0 & 0 & 2 & 0 \\ 0 & 0 & 0 & 0 & 0 & 2 \end{bmatrix} \tag{29}$$

$$T_{vert} = \begin{bmatrix} cos^2\phi_v & 0 & sin^2\phi_v & 0 & 2sin\phi_v cos\phi_v & 0 \\ 0 & 1 & 0 & 0 & 0 & 0 \\ sin^2\phi_v & 0 & cos^2\phi_v & 0 & -2sin\phi_v cos\phi_v & 0 \\ 0 & 0 & 0 & cos\phi_v & 0 & sin\phi_v \\ -sin\phi_v cos\phi_v & 0 & sin\phi_v cos\phi_v & 0 & cos^2\phi - sin^2\phi_v & 0 \\ 0 & 0 & 0 & -sin\phi_v & 0 & cos\phi_v \end{bmatrix} \tag{27}$$

$$T_{hori} = \begin{bmatrix} cos^2\theta_h & sin^2\theta_h & 0 & 2sin\theta_h cos\theta_h & 0 & 0 \\ sin^2\theta_h & cos^2\theta_h & 0 & -2sin\theta_h cos\theta_h & 0 & 0 \\ 0 & 0 & 1 & 0 & 0 & 0 \\ -sin\theta_h cos\theta_h & sin\theta_h cos\theta_h & 0 & cos^2\theta_h - sin^2\theta_h & 0 & 0 \\ 0 & 0 & 0 & 0 & cos\theta_h & sin\theta_h \\ 0 & 0 & 0 & 0 & -sin\theta_h & cos\theta_h \end{bmatrix} \tag{28}$$

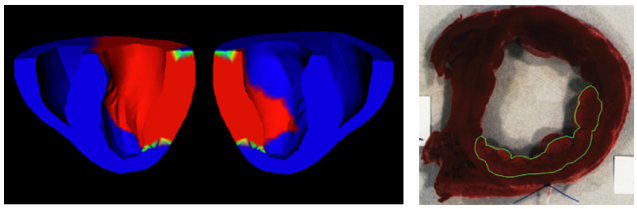

FIGURE 1. Left: Pathological case; part of the heart was assumed to be infarcted (red region). Right: TTC-stained post-mortem left-ventricular myocardium in which infarcted zone are highlighted.

2) GOVERNING EQUATIONS OF THE HEART SYSTEM

Specifically, under the assumption of Hooke's law, the total potential energy functional E of the system can be reached:

$$E = \frac{1}{2}\int_{\Omega} \sigma^T \epsilon d\Omega - \int_{\Omega} f^T u d\Omega \tag{30}$$

where f is the external force, which has detailed description in the following section. By using the strain-displacement equation $\varepsilon = \mathbf{LU}$ and minimizing the Equation (30) with respect to displacement, we can derive that the stiffness matrix K and force matrix F have the following form:

$$K_{I,J} = \int_{\Omega} {S_I}^T C S_J d\Omega \tag{31}$$

$$F_{I,J} = \int_{\Omega} \mathbf{N}_I^T f d\Omega \tag{32}$$

in the 2D case, with

$$\mathbf{N}_I = \begin{bmatrix} N_I & 0 \\ 0 & N_I \end{bmatrix}, \quad \mathbf{S}_I = \mathbf{LN_I} = \begin{bmatrix} N_{I,x} & 0 \\ 0 & N_{I,y} \\ N_{I,y} & N_{I,x} \end{bmatrix} \tag{33}$$

where $N_{I,x}$ and $N_{I,y}$ represent the derivatives of the MLS shape functions with respect to x and y, respectively. With regard to the 3D case,

$$\mathbf{N}_I = \begin{bmatrix} N_I & 0 & 0 \\ 0 & N_I & 0 \\ 0 & 0 & N_I \end{bmatrix} \tag{34}$$

$$S_I = \mathbf{LN}_I = \begin{bmatrix} N_{I,x} & 0 & 0 \\ 0 & N_{I,y} & 0 \\ 0 & 0 & N_{I,z} \\ N_{I,y} & N_{I,x} & 0 \\ 0 & N_{I,z} & N_{I,y} \\ N_{I,z} & 0 & N_{I,x} \end{bmatrix} \tag{35}$$

where $N_{I,x}$,$N_{I,y}$, and $N_{I,z}$ are the derivatives of the shape function with respect to x, y, and z, respectively.

3) EVALUATION OF SYSTEM INTEGRALS

To evaluate the entries of the system matrices, integrations over the problem domain and both the natural and the essential boundaries need to be be performed through numerical techniques such as the Gauss quadrature. A mesh of non-overlapping cells, called the background mesh, is required for the quadrature integration. In contrast to the FEM mesh needed for field variable interpolation, the background mesh, which needs to be properly designed to obtain an appropriate solution of desired accuracy, is used merely for the integration of the system matrices ([36]). Furthermore, the background cells are usually totally independent of the arrangement of nodes; in this paper, a regular-grid background mesh is used. In the regular-grid cell structure, there may exist cells that do not entirely belong to the analysis domain. This means that only a portion of such a cell belongs to the domain. A simple visibility scheme that automatically separates the portion of the cell that lies outside the physical domain is employed ([36]).

In the 2D case, we have used $m_c \times m_c$ cells in the integration, where $m_c = \sqrt{n_t}$ and n_t is the total number of nodes in the domain. The number of quadrature points depends on the number of nodes in a cell, and we have used $n_Q \times n_Q$ Gauss quadrature, where $n_Q = \sqrt{n_{node}} + 2$ and n_{node} is the number of nodes in a cell. In the 3D case, we have used $m_c \times m_c \times m_c$ cells, where $m_c = \sqrt{n_t}$ and n_t is the number of the nodal points ([36]). In each cell, we use $n_c \times n_c \times n_c$ Gauss quadrature.

D. EXTERNAL FORCES

Both imaging data information and prior modeling constraints, needed for the simultaneous recovery of the heart shape and motion, are incorporated in the external driving force term f, which has four primary components: (1) the data-driven edginess measures $F_{edginess}(\mathbf{x})$ of the myocardial boundary and tagging points, (2) the statistical prior distributions of the myocardial tissue locations $F_{prior}(\mathbf{x})$, (3) the temporal shape coherence measures on the image-derived salient features $F_{shape}(\mathbf{x})$, and (4) the motion constraints on the myocardial behavior $F_{temporal}(\mathbf{x})$, including the prior cyclic heart dynamics and the data-derived Eulerian velocity information.

For boundary and tagging line nodes, all four components contributes to the overall force field:

$$f_{boundary}(\mathbf{x}) = F_{edginess}(\mathbf{x})\,[\alpha(\mathbf{x})F_{prior}(\mathbf{x}) + \beta(\mathbf{x})F_{shape}(\mathbf{x}) + \gamma(\mathbf{x})F_{temporal}(\mathbf{x})] \tag{36}$$

Here, the algorithm favors locations that are likely edge points while maintaining the balance among the prior positional information, temporal filtering/prediction results, and salient shape coherence measures between frames. For all non-boundary/non-tag nodes, there are no constraints on them being edge points or preserving shape coherence between image frames. Therefore, the force term is simplified to

$$f_{other}(\mathbf{x}) = \alpha(\mathbf{x})F_{prior}(\mathbf{x}) + \gamma(\mathbf{x})F_{temporal}(\mathbf{x}) \tag{37}$$

All these four types of force components, $F_{edginess}(\mathbf{x})$, $F_{prior}(\mathbf{x})$, $F_{shape}(\mathbf{x})$, and $F_{temporal}(\mathbf{x})$, are normalized to the range of [0, 1], and the weighting constants $\alpha(\mathbf{x})$, $\beta(\mathbf{x})$, and $\gamma(\mathbf{x})$ are selected to reflect the varying data and model conditions in different parts of the heart at different time frames.

IEEE Journal of Translational Engineering in Health and Medicine

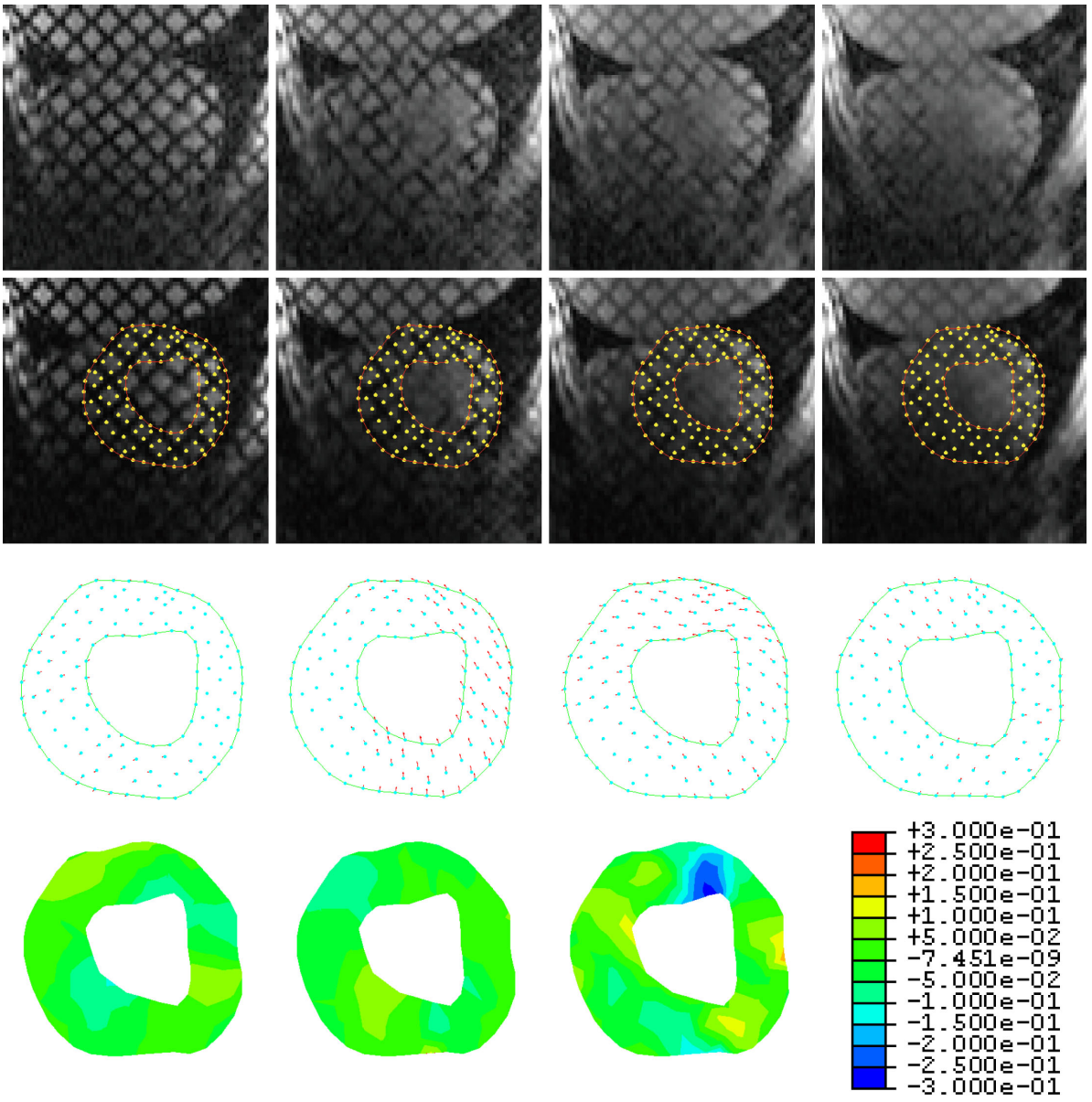

FIGURE 2. 1st row: Tagging images at frames #1, #5, #9, and #13; 2nd row: segmentation results at frames #1, #5, #9, and #13; 3rd row: estimated frame-to-frame displacement fields : between frames #1-2, #5-6, #9-10, and #13-14; 4th row: Strain estimates for tagging data between end-diastole and end-systole: radial, circumferential, shear strain, and scale map (from left to right).

1) BOUNDARY EDGINESS MEASURES

To achieve geometry recovery, the resulting boundary nodes (and some internal nodes for MRI tagging data) should be located at likely boundary (tagging line) locations. Earlier works have shown that portions of the heart boundary may have confusing gradient information caused by the partial volume effect and intensity homogeneity, thus achieving good segmentation results solely from gradient information is difficult. Furthermore, as suggested by ([28]), the diffusion of the gradient magnitude field generates a more robust gradient vector flow (GVF) with low GVF magnitude near the object boundary. Therefore, we construct our edginess measure to enforce high gradient values and low GVF values:

$$F_{edginess}(\mathbf{x}) = \frac{|GVF(\mathbf{x})|}{1 + |\bigtriangledown I(\mathbf{x})|} \tag{38}$$

where $\bigtriangledown I$ is image gradient and $|GVF|$is the GVF magnitude.

2) PRIOR SPATIAL DISTRIBUTIONS OF TISSUE ELEMENTS

To achieve more robust estimation results against imaging noises and defects, we impose constraining spatial ranges on the movement of the tissue elements. While these constraints are currently only enforced on the starting boundary and tag-

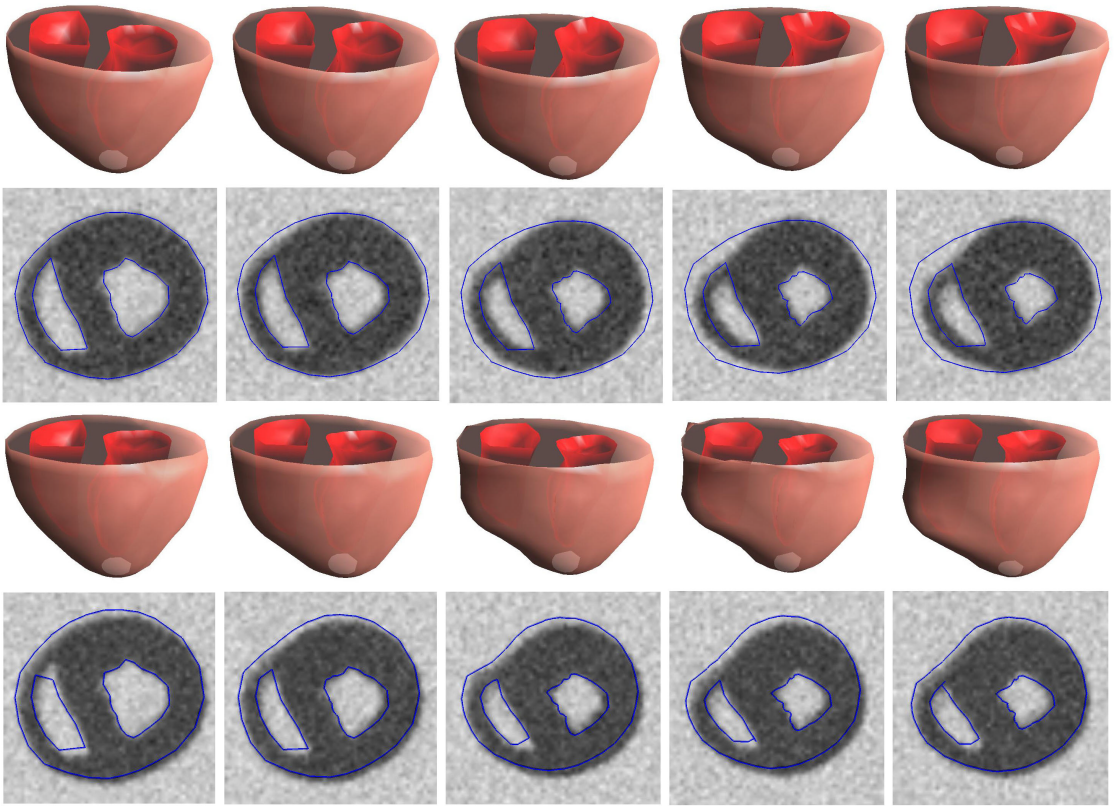

FIGURE 3. 1st and 2nd rows: Joint segmentation and motion tracking results with linear FEM framework. 3rd and 4th rows: Joint segmentation and motion tracking results with mesh-free framework. The 1st and 3rd rows show a selected segmented volume representation of the left and right ventricles. The 2nd row shows contours generated by a linear FEM-based method overlaid on the corresponding intensity image slice. The 4th row shows contours generated by the mesh-free method overlaid on the corresponding intensity image slice. The 2nd and 4th rows show how much the output of the algorithm matches the boundary in the image.

line nodes for each frame, there is little difference if we are considering the other nodes in the same fashion. The spatial prior ranges of the nodes are constructed as a 2D Gaussian distribution $\bar{N}(\mathbf{x}(k-1), \Sigma)$, where Σ is the variance, and the mean $\mathbf{x}(k-1)$ is the nodal point at the starting position of the current frame (result of the last frame). Therefore, the derived prior force component becomes

$$F_{prior}(\mathbf{x}) = 1 - \bar{N}(\mathbf{x}(k-1), \Sigma) \tag{39}$$

In 3D, we have

$$F_{prior}(\mathbf{x}) = 1 - \bar{N}(\mathbf{x}(k-1), \Sigma_1, \Sigma_2, \Sigma_3) \tag{40}$$

where $\bar{N}(\mathbf{x}(k-1), \Sigma_1, \Sigma_2, \Sigma_3)$ is the 3D Gaussian distribution as the spatial prior range.

Obviously, we assume that every node moves away from its starting position during a cardiac cycle. While this has produced reasonable results in our experiments, other types of biases can be used as long as they are meaningful to the specific cases.

3) SHAPE COHERENCE MEASURES

Earlier efforts have demonstrated and validated the effectiveness of tracking the heart boundary motion by using geometrical shape cues ([37], [38]). Following this strategy, we propose to use the shape coherence of the myocardial salient landmarks, such as boundary nodes and tag-tag/tag-boundary crossings, between image frames as an additional guideline for constructing the force field. Based on the theorem of implicit iso-intensity curve representation ([39]), the differential curvature values of the nodes from the images can be directly computed in the two-dimensional case:

$$\kappa(\mathbf{x}) = \frac{I_{yy}(\mathbf{x})I_x^2(\mathbf{x}) - 2I_{xy}(\mathbf{x})I_x(\mathbf{x})I_y(\mathbf{x}) + I_{xx}(\mathbf{x})I_y^2(\mathbf{x})}{(I_x^2(\mathbf{x}) + I_y^2(\mathbf{x}))^{3/2}}$$

where I_x and I_y are the first derivatives of the image intensity, and I_{xx}, I_{yy}, and I_{xy} are the second derivatives.

In the 3D case, the Hessian matrix can be derived as

$$\mathbf{H} = \begin{bmatrix} I_{xx} & I_{xy} & I_{xz} \\ I_{xy} & I_{yy} & I_{yz} \\ I_{xz} & I_{yz} & I_{zz} \end{bmatrix} \tag{41}$$

where I_{xx}, I_{xy}, I_{xz}, I_{yy}, I_{yz}, and I_{zz} are the second derivatives of the 3D image intensity. After rotating the Hessian to align the first axis with the gradient $g = (I_x, \ I_y, \ I_z)$, the resulting

IEEE Journal of Translational Engineering in Health and Medicine

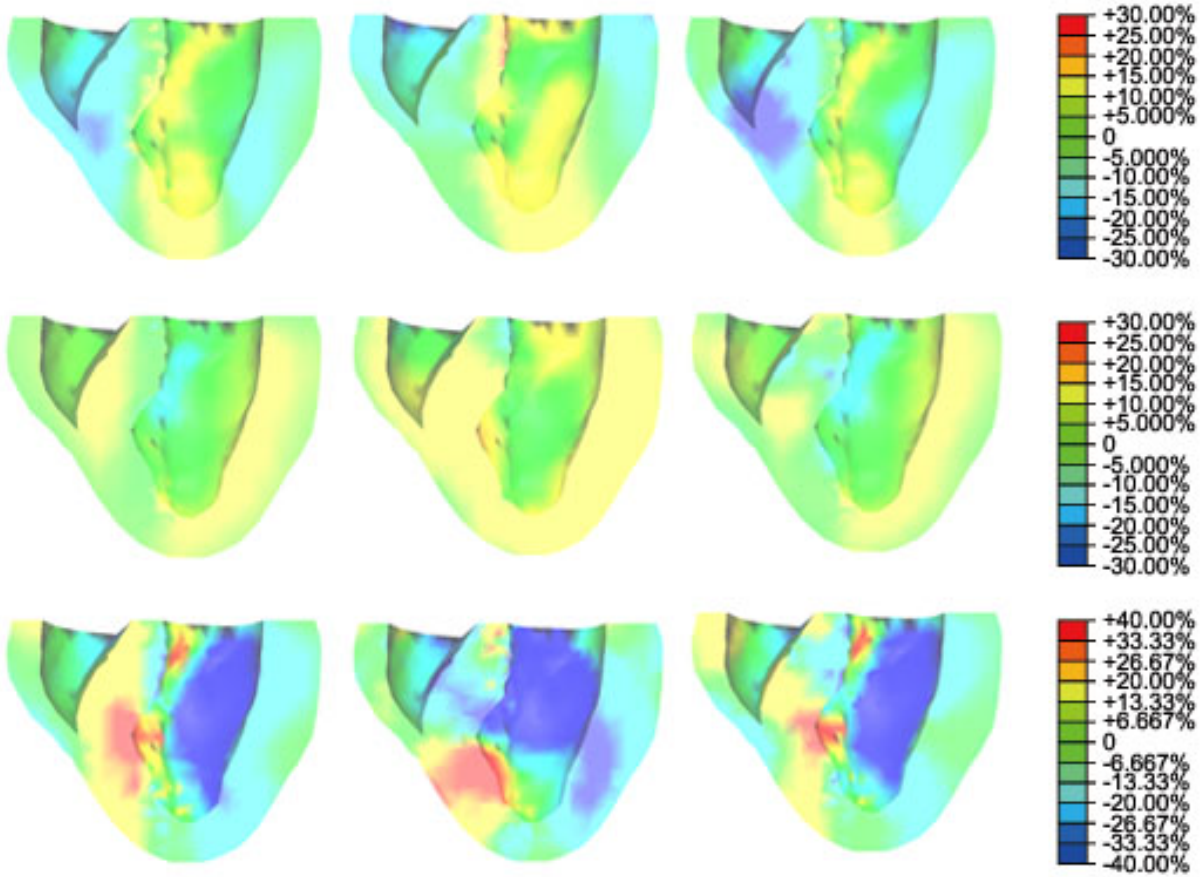

FIGURE 4. A long-axis cut-away view of the heart showing strains at frame #25 with respect to the #1 frame. Top to bottom: radial strain maps, circumferential strain, and longitudinal strain. Left to right: ground truth, FEM results, Mesh-free results, and scale map.

matrix $\mathbf{H}^r$ can be written as

$$\mathbf{H}^r = \begin{bmatrix} I_{gg} & & \\ \cdots\cdots & \cdots\cdots & \\ & I_{uu} \quad I_{uv} & \\ & I_{uv} \quad I_{vv} & \end{bmatrix} = \begin{bmatrix} I_{gg} & \\ \cdots\cdots & \\ & \mathbf{H_t}^r \end{bmatrix} \tag{42}$$

Assuming that the eigenvalues of $\mathbf{H_t}^r$ are λ_1 (maximum) and λ_2 (minimum), the corresponding principle curvatures can be obtained:

$$\kappa_1 = \frac{-\lambda_1}{\|g\|} \tag{43}$$

$$\kappa_2 = \frac{-\lambda_2}{\|g\|} \tag{44}$$

Therefore, the mean curvature can be computed as

$$\kappa(\mathbf{x}) = \frac{1}{2}(\kappa_1 + \kappa_2) \tag{45}$$

Then, the basic idea is to use the minimum bending energy criterion to guide the boundary and tag nodes moving toward the final pixel positions, which have as close geometric properties as these nodes at the previous frame (starting nodal positions for the current frame). Therefore, the shape force term is defined as

$$F_{shape}(\mathbf{x}) = |\kappa((\mathbf{x} + \delta\mathbf{x})(k+1)) - \kappa((\mathbf{x}(k))| \tag{46}$$

where $\kappa((\mathbf{x} + \delta\mathbf{x})(k+1))$ and $\kappa((\mathbf{x}(k))$ are the iso-intensity curvatures at frame $k+1$ and k, respectively, and $\delta\mathbf{x}$ indicates that the search is conducted at a local window near the original boundary/tag point $\mathbf{x}$.

4) TEMPORAL FILTERING AND PREDICTION: EULERIAN KINEMATICS DATA AND CYCLIC MOTION MODEL

As with most other cardiac applications, we assume that the motion of the heart is periodic. We can expand the trajectory of each node into sine functions ([40]). Owing to the limited temporal resolution available, the first two terms of the expansion are retained and a continuous model of the trajectory of any mesh node is approximated by a closed ellipse in a short time interval in a piecewise sense:

$$\mathbf{x}(t) = \bar{\mathbf{x}} + A\sin(2\pi\omega t + \varphi) \tag{47}$$

where t is the continuous time index, $\mathbf{x}$ is the node position, $\bar{\mathbf{x}}$ is the mean position over the cardiac period, and A is the amplitude of the motion. The frequency of the oscillator is $2\pi\omega = 2\pi/T$, where T is the period of the cardiac cycle, which is known from the imaging data.

An estimation of the node $\mathbf{x}$ at frame $k+1$ can be provided by the past positions of a given node $\mathbf{x}$ up to the current image frame k and the available imaging/image-derived Eulerian

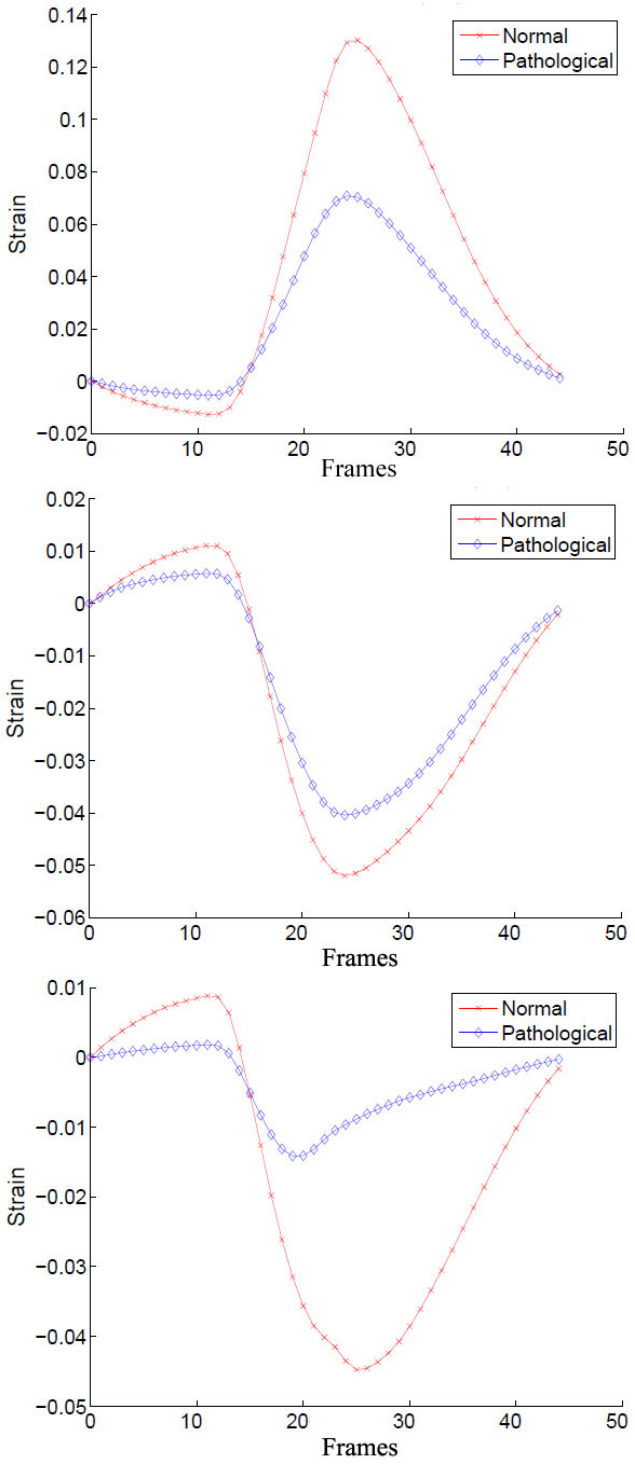

FIGURE 5. **The mean strains between the normal and the pathological cases by using the proposed method: radial strain (top), circumferential strain (middle), and longitudinal strain (bottom).**

motion information. Typical Eulerian kinematic data include the optical flow field calculated from image frames k and $k+1$, the instantaneous velocity provided by MR phase contrast images, the partial velocity information from Doppler echocardiography, etc. A standard Kalman filter/predictor can be used to estimate the state variables (position, displacement, and velocity) at frame $k+1$ as follows:

$$\hat{z}(k+1 \mid k) = \bar{C}\hat{z}(k \mid k) \tag{48}$$

with

$$\bar{C} = \begin{bmatrix} \lambda & \mu & 0 \\ 1-\cos(\omega\triangle t) & \cos(\omega\triangle t) & \frac{1}{\omega}\sin(\omega\triangle t) \\ \omega\sin(\omega\triangle t) & -\omega\sin(\omega\triangle t) & \cos(\omega\triangle t) \end{bmatrix}$$

where $z = [\bar{\mathbf{x}}, \mathbf{x}, \dot{\mathbf{x}}]$ is the state vector, $\hat{z}(k+1 \mid k)$ is the Kalman filter estimated state for image frame $k+1$, $\hat{z}(k \mid k)$ is the estimated state vector up to frame k, $\lambda = (n-1)/n$ and $\mu = 1/n$ are constants, and n is the number of image frames over the heart cycle. In our experiments, the velocity term in Equation (48) adopts the available Eulerian motion fields from the MR phase contrast velocity images or the spatiotemporal intensity flow between MR image frames. For phase velocity data, the regularization of the vector field may be needed to remove noise.

The temporally predicted possible node position $\hat{\mathbf{x}}$ is used to construct a rotated 2D Gaussian distribution $\bar{N}(\hat{\mathbf{x}}, \Sigma_i, \Sigma_j, \theta(\hat{\mathbf{x}}))$, where Σ_i and Σ_j are the variances in the rotated major directions, and θ is the angle of the line formed by $\mathbf{x}(k-1)$ and $\hat{\mathbf{x}}(k)$ with respect to the $x-$axis, with k and $k-1$ indicating image frame numbers. We can construct the temporal filtering/prediction force as

$$F_{temporal}(\mathbf{x}) = 1 - \bar{N}(\hat{\mathbf{x}}, \Sigma_i, \Sigma_j, \theta(\hat{\mathbf{x}})) \tag{49}$$

In the 3D case, the temporal force could be constructed as follows:

$$F_{temporal}(\mathbf{x}) = 1 - \bar{N}(\hat{\mathbf{x}}, \Sigma_i, \Sigma_j, \Sigma_k, \theta(\hat{\mathbf{x}}), \phi(\hat{\mathbf{x}})) \tag{50}$$

$\bar{N}(\hat{\mathbf{x}}, \Sigma_i, \Sigma_j, \Sigma_k, \theta(\hat{\mathbf{x}}), \phi(\hat{\mathbf{x}}))$ is a rotated 3D Gaussian distribution, where Σ_i, Σ_j, and Σ_k are the variances in the rotated major directions, and θ and ϕ are the angles of the line formed by $\mathbf{x}(k-1)$ and $\hat{\mathbf{x}}(k)$ with respect to the Cartesian coordinate.

III. EXPERIMENTAL VALIDATION AND EVALUATION

With the mesh-free particle framework for the simultaneous recovery of the heart shape and motion, we have performed experiments on synthetic data, MR phase contrast images including instantaneous velocity information sequences, MR tagging sequences, and gradient echo cine MR image sequences. The proposed framework can employ the measured data extracted from images, which are either intensity or/and velocity depending on the imaging protocol used.

The first step of the algorithm is initialization which includes extraction of the useful features (such as endo- and epi- boundaries and tag-tag points) of the first frame and allocation of the sampling nodes bounded by the initial boundaries. A local analysis domain centered at each node is determined. Then based on the MLS approximations, the shape interpolation functions are constructed and the stiffness matrix K and external force terms are formulated. Finally,

IEEE Journal of Translational Engineering in Health and Medicine

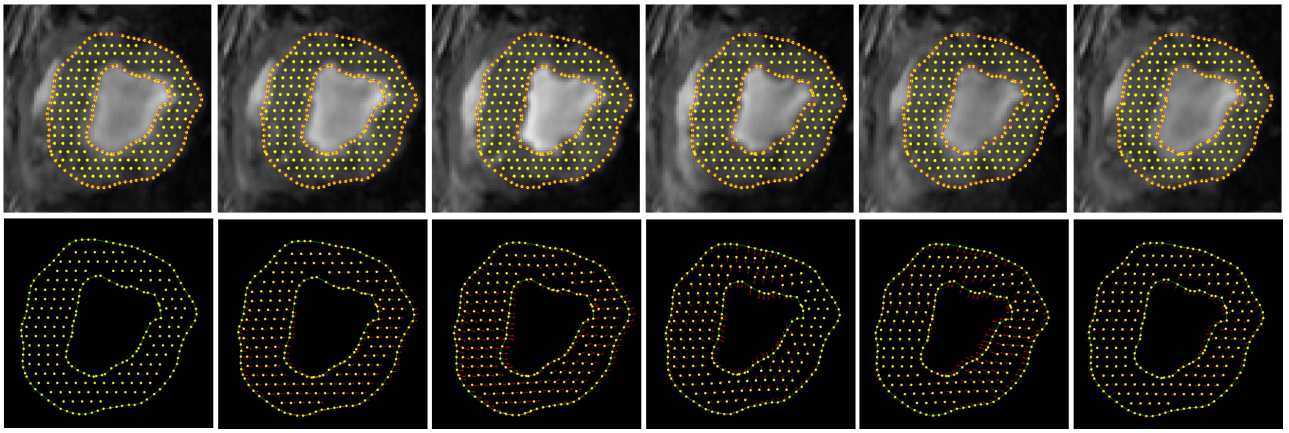

FIGURE 6. 1st row: Selected Segmentation results for MR phase contrast image at frames #1, #3, #6, #9, #12, and #15. 2nd row: Estimation of the displacement vector maps with respect to frame #1 for the MR phase contrast images at frames #3, #6, #9, and #12.

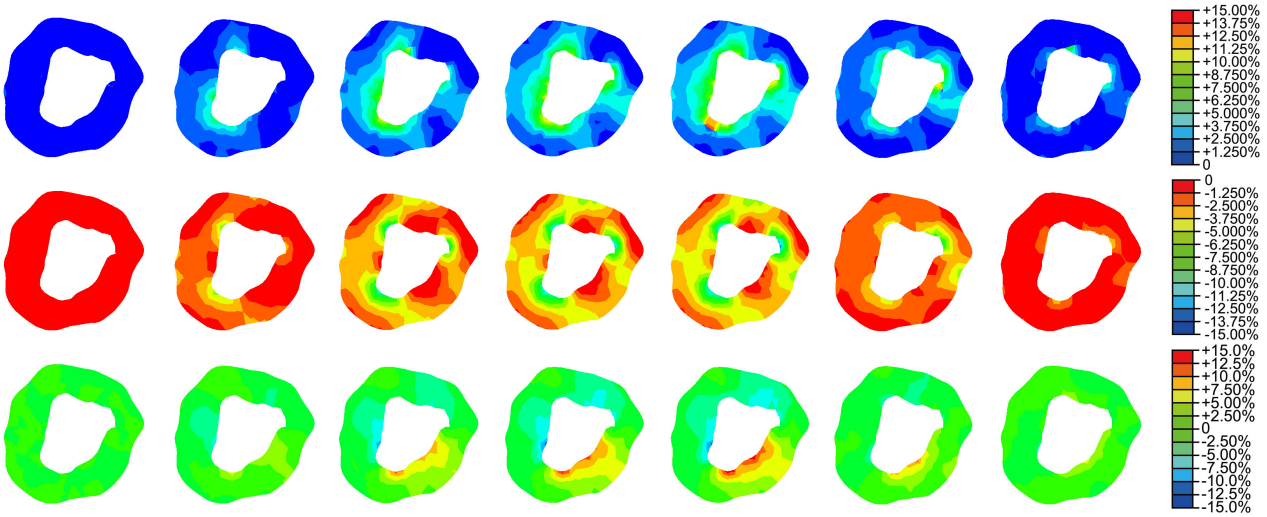

FIGURE 7. 1st row: Estimation results of the radial strain maps for the MR phase contrast images (w.r.t. frame #1, the end-diastolic phase) at frames #1, #6, #8, #9, #10, #14, and #16. 2nd row: Joint estimation results of the circumferential strain maps for the MR phase contrast images (w.r.t. frame #1, the end-diastolic phase) at frames #1, #6, #8, #9, #10, #14, and #16. 3rd row: Joint estimation results of the radial-circumferential shear strain maps for the MR phase contrast images (w.r.t. frame #1, the end-diastolic phase) at frames #1, #6, #8, #9, #10, #14, and #16.

we estimate the dense displacement field by tracking for minimizing the total energy between successive frames.

A. SYNTHETIC DATA

The canine heart model of the University of Auckland, which provides both the cardiac geometry and the fiber architecture obtained through anatomical experiments ([34]), was used to generate the synthetic data. Young's moduli along and across the fiber were 75 and 25 kPa, respectively. Poisson's ratio was set to 0.47 to simulate incompressibility. The physiome model was applied to the heart model to provide the ground truth, and 50 frames of one cardiac cycle were obtained, which were then converted into a grayscale structural image sequence of 50 frames with image size of $75 \times 75 \times 16$ and spatial resolution of $1.27 \times 1.27 \times 4.86mm^3$. Noise with 5dB SNR was added to the derived images data to provide noisy measurements.

The epicardial and endocardial surfaces of the whole heart segmented from the synthetic images in the first frame as well as 1274 myocardial sample points formed the mesh-free representation of the heart. For the purpose of comparisons, we also constructed a finite element model with 2083 points and 10824 tetrahedrons. The shape and kinematic parameters of the synthetic heart were recovered by the proposed approach with mesh-free (linear bases, without refinement) and FEM (linear tetrahedral elements, without refinement) representations under the same external forces. Further, the fiber orientations were obtained by invasive procedures of dead canine hearts ([35]). The data are in 3D and are obtained at the most relaxed state of the heart. In the next canine experiment, 2D mid-ventricle slice data were extracted for our initial fiber orientations. The 2D fiber orientation data are mapped to our myocardium geometry by using principal warps.

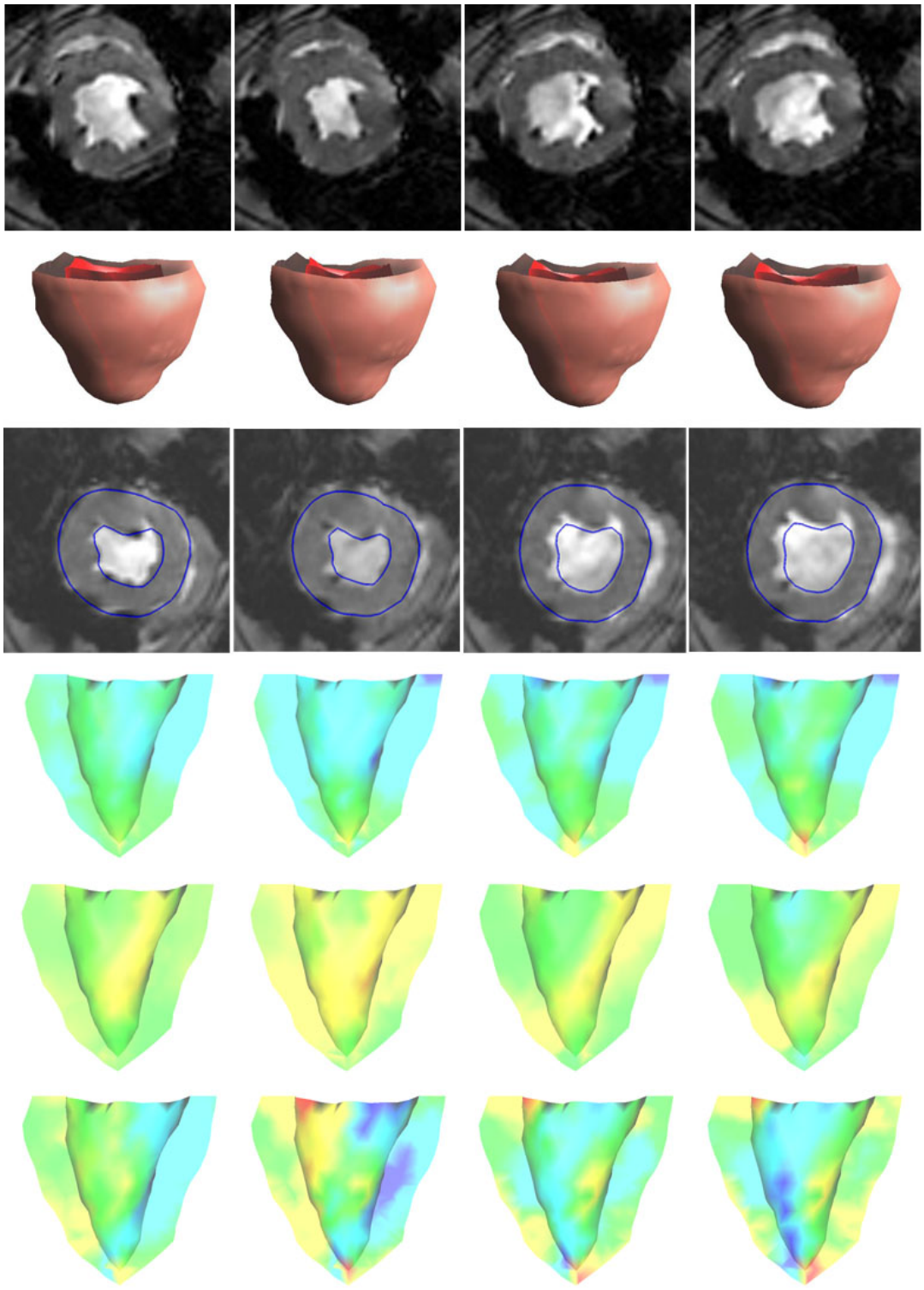

FIGURE 8. Canine data experimental results using meshfree framework. Top row: original 2D image. 2nd row: selected volume segmentation results. 3rd row: segmentation results (blue contours) overlaid on the original image. 4th to 6th row: A long-axis cut-away view of the LV showing radial (4th row), circumferential (5th row) and longitudinal strain (6th row) at frames #3, #6, #11, and #13 with the same scale as shown in Fig. 4.

Apart from the normal case, a validation with a pathological case was also performed. In the pathological case, part of the heart was assumed to be infarcted (see the left of Fig.1), where Young's modulus was set to be three times that in the normal case. Then, procedures similar to those described above were used. Finally, the shape and

IEEE Journal of Translational Engineering in Health and Medicine

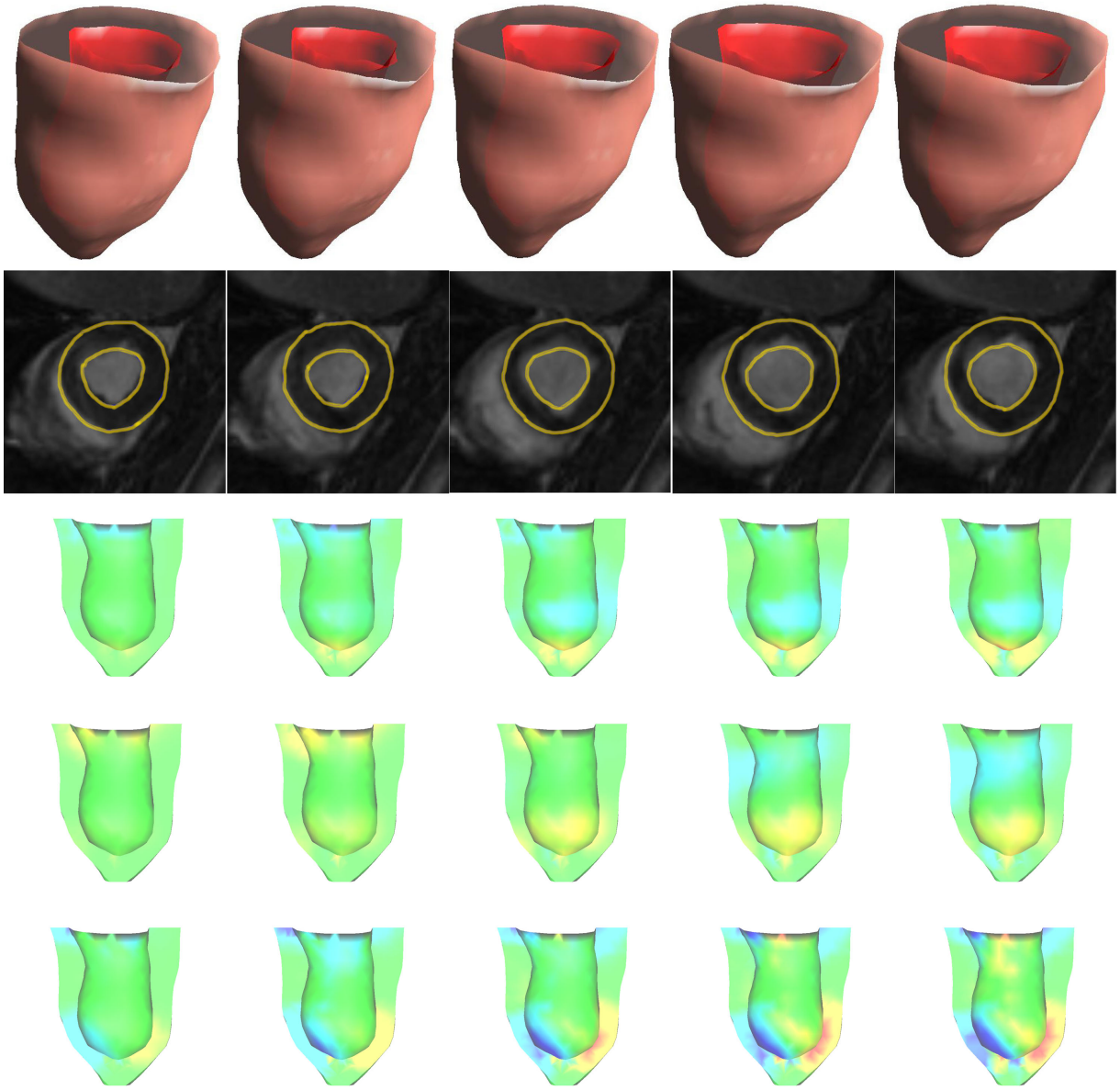

FIGURE 9. Mini- porcine1 experimental results at frames #3, #6, #9, #12, and #16 using meshfree framework. Top row: selected volume segmentation results. 2nd row: segmentation results (yellow contours) overlaid on the original image. 3rd to 5th row: A long-axis cut-away view of the LV showing radial (3rd row), circumferential (4th row) and longitudinal strain (5th row) at corresponding 5 time points with the same scale as shown in Fig. 4.

kinematic parameters of the synthetic heart were recovered by the proposed approach with mesh-free representation under the same biomechanical model as in the normal case.

In the third experiment, the joint method and the traditional separated strategy ([20]) were compared using the pathological simulation results.

B. MRI PHASE CONTRAST IMAGE SEQUENCES

A set of canine MR phase contrast image sequences has been used in this experiment. During the animal experiment, a proximal segment of the left anterior descending (LAD) coronary artery of an adult mongrel dog is dissected free to enable the production of a controlled, graded coronary stenosis.

Sixteen canine MR phase contrast velocity and magnitude images are acquired over the heart cycle, with the following imaging parameters: flip angle $=$ $30°$, TE $=$ $11ms$, TR $=$ $34ms$, FOV $=$ $28cm$, matrix 256×128, and venc $=$ $15cm/s$. The image resolution is $1.09mm/pixel$, and the velocity intensity ranges from $-150mm/s$ to $150mm/s$, with the signs indicating the directions.

The histological staining of the post-mortem myocardial tissues is shown in right of Fig. 1, and the infarct regions is highlighted. It provides the clinical gold standard for the assessment of the image analysis results.

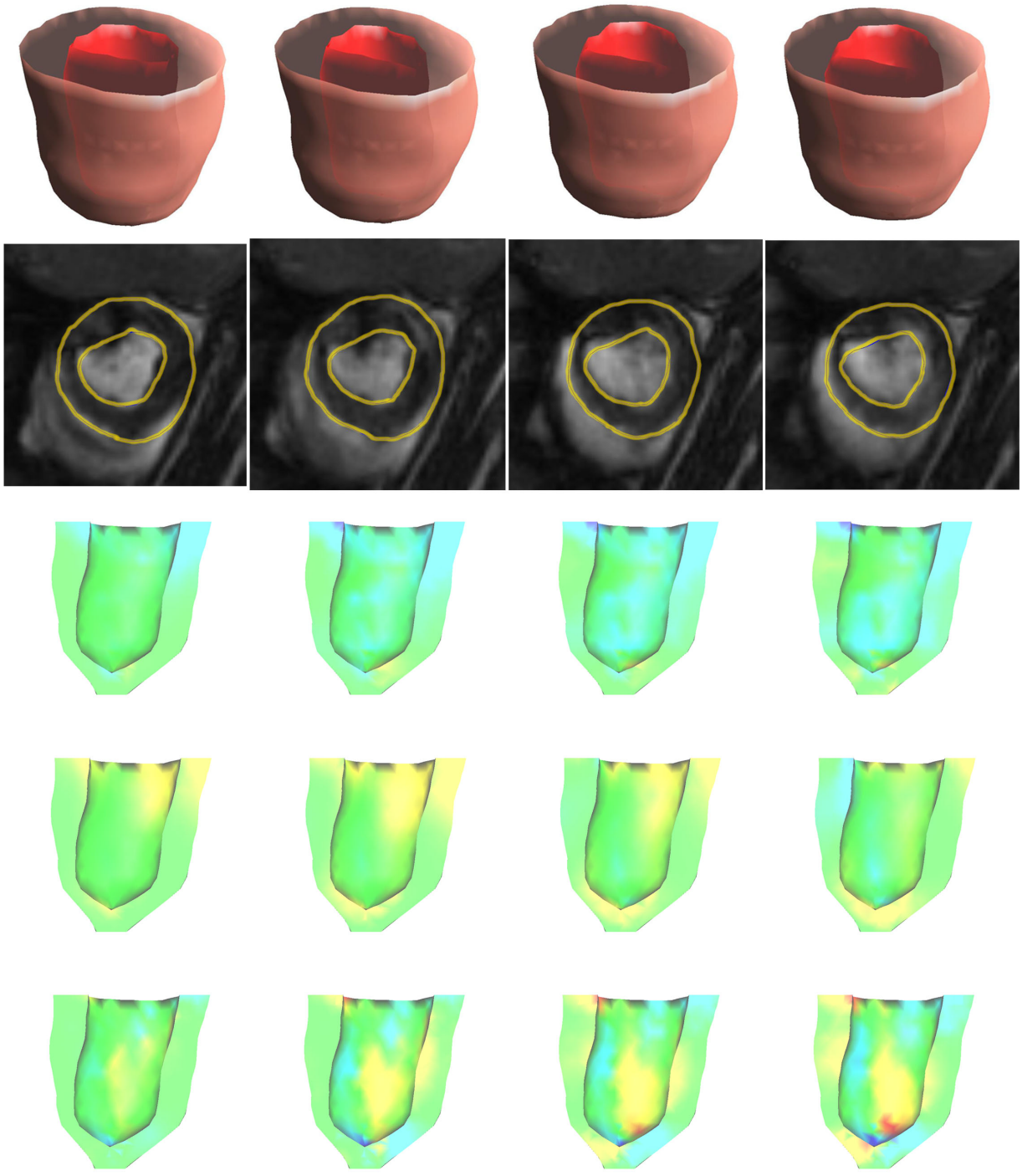

FIGURE 10. Mini- porcine2 experimental results at frames #3, #6, #9, and #12 using meshfree framework. Top row: selected volume segmentation results. 2nd row: segmentation results (yellow contours) overlaid on the original image. 3rd to 5th row: A long-axis cut-away view of the LV showing radial (3rd row), circumferential (4th row) and longitudinal strain (5th row) with the same scale as shown in Fig. 4.

C. MR TAGGING IMAGE SEQUENCE

Sixteen MR tagging images of a healthy mongrel dog over the heart cycle are used in the second experiment, where the tagging magnetic void grid is applied at the end diastole (frame #1), shown in Fig. 2.

D. GRADIENT ECHO CINE MR IMAGE SEQUENCE

We also implemented our approach on gradient echo cine MR image sequence, including animals and humans: 1 normal dog, 2 mini-porcine, and 22 human volunteers. The corresponding image parameters are summarized in Table. 1.

IEEE Journal of Translational Engineering in Health and Medicine

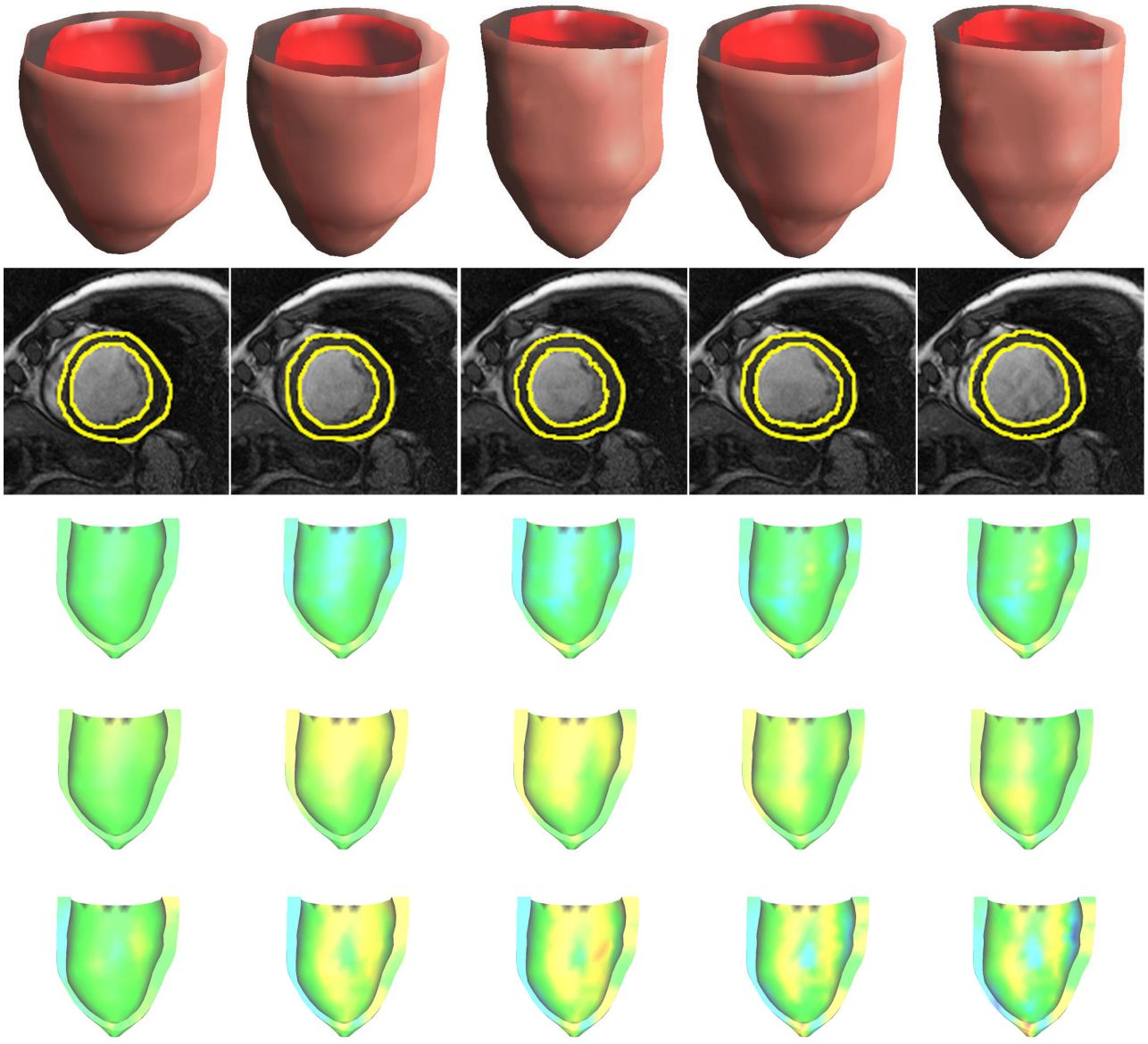

FIGURE 11. Patient 1's experimental results at frames #3, #6, #9, #12, and #16 by using mesh-free framework. Top row: selected volume segmentation results. 2nd row: segmentation results (blue contours) overlaid on the original image. 3rd to 5th rows: a long-axis cut-away view of the LV showing radial (3rd row), circumferential (4th row), and longitudinal (5th row) strains with the same scale as that used in the 1st row of Fig. 4.

The myocardium is modeled as a transversely linear elastic solid, as described in section 2.3. The fiber orientations are obtained using Guccione et al.'s model ([41]).

IV. RESULTS AND DISCUSSIONS

A. QUANTITATIVE ANALYSIS OF SYNTHETIC DATA

Fig. 3 shows the results under the linear FEM framework and those under the mesh-free framework. Table 2 shows the quantitative assessments of the average positional errors (Error is defined as the distance between the estimated boundary point and its corresponding true one. Each datum represents the mean $\pm$ standard deviation.). Overall, the results obtained with the mesh-free representation agree with the ground truth. It can be seen that the segmented shape of the whole heart with the mesh-free representation is closer to the boundary defined in the image. In Fig. 4, for frame #25 as an example, it can be seen that the strains estimated using the mesh-free representation are better; the strain is smoother, and its distribution is similar to the ground truth. This is mainly because the mesh-free representation can handle fiber discontinuities and avoid the problem caused by tetra skewing. In the reported experiments on a 2.33 GHz 4-core computer with 8 GB memory and under the Matlab environment, each iteration loop took 491 s for the mesh-free method and 478 s for the FEM method. Please note that especially for complex geometries like the heart, the

TABLE 1. The imaging parameters used for experiments.

Data	Resolution (mm)	Image size	Slices	Frames
Canine	$1.56 * 1.56 * 5.0$	$64 * 64$	16	16
mini-porcine 1	$1.25 * 1.25 * 8.0$	$64 * 64$	12	20
mini-porcine 2	$1.25 * 1.25 * 8.0$	$64 * 64$	16	20
Patient	$1.27 * 1.27 * 8.0$	$128 * 128$	18	20

TABLE 2. Average positional errors over time. Each data cell represents the mean and standard deviational errors.

Frame	Average errors (Mean $\pm$ Standard Deviation) (pixel)	
	FEM	Mesh-free
2	1.17 ± 0.62	1.17 ± 0.58
8	1.19 ± 0.73	1.17 ± 0.62
14	1.20 ± 0.88	1.19 ± 0.77
20	1.74 ± 0.94	1.21 ± 0.78
26	1.98 ± 1.0	1.23 ± 0.86
32	2.57 ± 0.99	1.25 ± 0.87
38	3.14 ± 1.1	1.30 ± 0.98
44	4.61 ± 1.2	1.31 ± 0.98
50	5.64 ± 1.3	1.33 ± 0.99

TABLE 3. Mean strains in different segments. The 16 segments are sorted by the mean of the largest principal strains in ascending order. Infarcted regions are (1, 5, 6, 7, 12).

Our method	Traditional strategy ([20])
(1) 0.079	(5) 0.091
(5) 0.084	(11) 0.120
(6) 0.092	(1) 0.130
(11) 0.116	(6) 0.135
(12) 0.120	(12) 0.136
(7) 0.125	(8) 0.138
(2) 0.131	(2) 0.144
(8) 0.134	(7) 0.147
(16) 0.142	(13) 0.149
(13) 0.147	(16) 0.152
(4) 0.157	(4) 0.161
(3) 0.159	(3) 0.166
(9) 0.163	(14) 0.199
(10) 0.170	(10) 0.207
(14) 0.201	(9) 0.231
(15) 0.243	(15) 0.267

time required for constructing the mesh in FEM may even be longer than that required for the analysis itself.

The strain plots in Fig. 5 show a comparison of the mean strains between the normal and the pathological cases by using the proposed method; this figure shows that all strain changes in the pathological case are smaller than those in the normal case because of the infarction. These results demonstrate that our method can show pathological behaviors to some extent.

In the third experiment, to perform a quantitative comparison, we computed the mean strains in different segments and sorted them in ascending order (Table 3). The strains used were the largest principal strains. From the table, we can see that our proposed framework gives the best performance. First, almost all infarcted segments (1, 5, 6, 7, and 12) are located at the beginning of the queue. Second, the segments directly neighboring the infarcted ones are at the front of the queue. This is because shape/kinematics recovery is constrained in a unified framework, which gives a more consistent result. More importantly, the traditional strategy requires isolation of the myocardium from the background information throughout the cardiac cycle before processing. This segmentation step is difficult and cannot be done automatically, and thus, the time required for segmenting and establishing a sparse set of corresponding feature points between boundaries may even be longer than that required for the motion tracking itself.

B. VALIDATION WITH TTC-STAINED RESULTS

The 1st row of Fig. 6 shows volumetric segmentation results from the phase contrast data which are visually robust and sensible. The detected boundary contours have consistent spatial and temporal characteristics, which are much desired for image sequence segmentation and for motion analysis. Further, the recovered motion measures from the image sequence are presented for displacement vector fields in the 2nd row of Fig. 6 and for cardiac-specific radial strain maps (1st row of Fig. 7, indicator for myocardial contraction), circumferential strain maps (2nd row of Fig. 7, indicator for myocardial twisting), and shear strain maps (3rd row of Fig. 7), all with respective to the end-diastolic image frame. From the displacement vectors, it can be observed that during the contraction phase of the cardiac cycle (i.e., frames #1 to #8), there is little contracting motion at the infarct zone (lower right part) until frame #6. At the beginning of the cardiac expansion phase (frames #9 to #10), however, the contracting motion of the infarcted tissues continues while the expanding motion of the normal tissues just starts. The expansion at the infarct zone does not occur until frame #14. From the strain maps, the changes in the deformation parameters (signs and magnitude) can be detected. It is quite obvious that the infarct region has vastly different characteristics from the normal zones: little deformation in the radial and circumferential directions, and opposite changes in the shear strain maps. These signs of dyskinesias (impairment of voluntary movements resulting in fragmented or jerky motions) and motion reductions at the lower-right part of the LV are clear indications of myocardial injury, and they agree with the histochemical result very well.

C. MR TAGGING IMAGE SEQUENCE

The volumetric segmentation results are shown in Fig. 2. The cardiac-specific strain maps are also given in Fig. 2 between the end- diastole (ED) and end-systole (ES) frames. Because the tagging grid decays over time, the tag lines in the images become very weak late in the image sequence. This hinders the reliable segmentation and tracking of the LV boundary and tagging points. Further efforts on constructing appropriate external forces are needed and in progress, including the modeling of the temporal intensity changes of the tag line and the use of directional band-pass filters to enhance tag line contrast.

D. GRADIENT ECHO CINE MR IMAGE SEQUENCE

The volumetric segmentation results, namely, the estimated displacement vector map with respect to end-diastole are

IEEE Journal of Translational Engineering in Health and Medicine

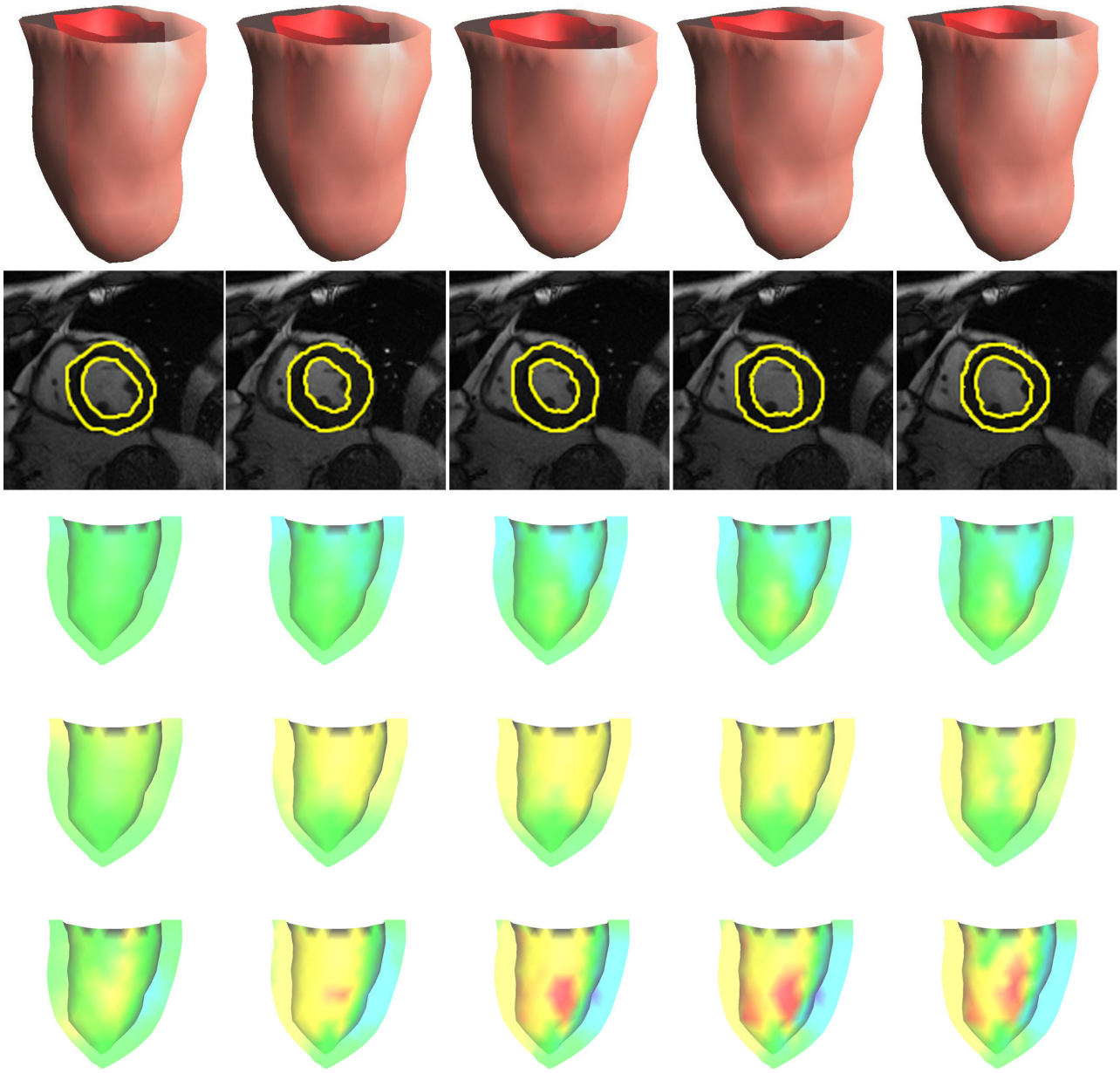

FIGURE 12. Patient 2's experimental results at frames #3, #6, #9, #12, and #16 by using mesh-free framework. Top row: selected volume segmentation results. 2nd row: segmentation results (blue contours) overlaid on the original image. 3rd to 5th rows: a long-axis cut-away view of the LV showing radial (3rd row), circumferential (4th row), and longitudinal (5th row) strains with the same scale as that used in the 1st row of Fig. 4.

shown in the Fig. 8-12. As expected, we see substantially more movement by the endocardial tissue than the epicardial tissue. To the end, we have calculated the strain tensors for each point to depict the non-rigid deformation. The radial, circumferential, and longitudinal strain maps are also given in Fig. 8-12, all with respect to the end-diastolic frame.

From the strain maps, we can see that the endocardial tissue deforms more than the epicardial tissue in the radial and circumferential directions. Further, it is quite obvious that during the cardiac deformation from ED to ES,the magnitudes of the radial, circumferential, and longitudinal strains increase, in which the longitudinal strains are relatively small. This indicates that the myocardium is primarily thickened in the radial direction and shortened in the circumferential direction.

For the human experiments, most of the trajectories obtained using the mesh-free method are converged. From the segmentation result and the trajectory of the boundary points, we can see that the mesh-free framework is more suitable for segmentation than the FEM representation. This is because it needs no remeshing, and a more accurate result can be obtained only by changing the weighting function. The strain

TABLE 4. Average and maximum distances between automatic and manual contours (pixel).

Average	endo	1.01 ± 0.53
	epi	0.92 ± 0.32
Maximum	endo	3.31
	epi	2.86

distribution of the model recovered by the mesh-free method agrees with the observations available from biomechanics and cardiology literatures, and this distribution is continuous. These promising results demonstrate that the proposed algorithm can be used to perform 3D segmentation and motion tracking simultaneously.

To validate the success of the proposed segmentation procedure, we compared the results of the human experiments with manual segmentation from cardiac MRI images of 22 patients. Table 4 summarizes the means and standard deviations of the position differences between the results of the proposed algorithm and manual contours. These numbers show that, globally, the automatic segmentations are very close to the manual ones.

V. CONCLUSIONS AND PERSPECTIVES

We have proposed spatiotemporal strategies for the joint segmentation and motion tracking of the heart. This unified approach is based on the use of image analysis strategies and mechanical modeling of the myocardium, and it is implemented in a mesh-free framework for the integration of complementary image sources.

This joint segmentation and motion analysis framework estimates the optimal shape, motion, and deformation parameters from noisy image data. Image-derived information serves as the external force. The application of a continuum mechanical model of the myocardium provides physically meaningful constraints on the dynamic behaviors of the heart tissue.

We should note that there are several parameters (weighting parameters (α, β, and γ), variance parameters (Σ_1, Σ_2, and Σ_3)) in the proposed method. The incorrect selection of these parameters will result in large estimation errors or even divergence. A general rule on the choice of these parameters is related to the confidence measures on the available imaging/imaging-derived measurement data. For example, if we trust F_{shape} more than the F_{prior}, we should make α smaller than β. This will deemphasize the importance of F_{prior} relative to F_{shape}. An automatic procedure to determine the algorithm parameters obtained from the local phase coherence ([42]) of images is under investigation.

The algorithms in this paper only provide the quantitative estimation of the possible locations and extents of the infarcted area, but not the material properties, such as Young's moduli of the diseased areas, that have great clinical value. Further research could extend to joint segmentation, motion, and a material parameters estimation framework.

Moreover, from the viewpoint of biomechanical constraints, although we have adopted anisotropic material models, these remain different from the extremely complex physical properties of an actual heart. First, while most works thus far have used linear material models of the heart muscles under infinitesimal stain theory, we believe that the adopted constrained biological model of the heart with large deformation will provide more accurate estimation results. Furthermore, integrating electrical activation into the biomechanical model would be very useful to help estimate the shape and motion parameters from cardiac image sequences ([13]).

ACKNOWLEDGMENT

The authors would like to thank Dr. Albert Sinusas of Yale University for the canine experiments and imaging data. They also thank the reviewers for their comments and suggestions.

REFERENCES

[1] H. Wang and A. A. Amini, "Cardiac motion and deformation recovery from MRI: A review," *IEEE Trans. Med. Imag.*, vol. 31, no. 2, pp. 487–503, Feb. 2012.

[2] J. Milles, R. J. V. D. Geest, M. Jerosch-Herold, J. H. C. Reiber, and B. P. F. Lelieveldt, "Fully automated motion correction in first-pass myocardial perfusion MR image sequences," *IEEE Trans. Med. Imag.*, vol. 27, no. 11, pp. 1611–1621, Nov. 2008.

[3] A. Frangi, W. J. Niessen, and M. A. Viergever, "Three-dimensional modeling for functional analysis of cardiac images, a review," *IEEE Trans. Med. Imag.*, vol. 20, no. 1, pp. 2–25, Jan. 2001.

[4] A. Suinesiaputra *et al.*, "A collaborative resource to build consensus for automated left ventricular segmentation of cardiac MR images," *Med. Image Anal.*, vol. 18, no. 1, pp. 50–62, 2014.

[5] U. Kurkure, A. Pednekar, R. Muthupillai, S. D. Flamm, and I. A. Kakadiaris, "Localization and segmentation of left ventricle in cardiac cine-MR images," *IEEE Trans. Biomed. Eng.*, vol. 56, no. 5, pp. 1360–1370, May 2009.

[6] M. Lorenzo-Valdes, G. I. Sanchez-Ortiz, R. Mohiaddin, and D. Rueckert, "Atlas-based segmentation and tracking of 3D cardiac MR images using non-rigid registration," in *Medical Image Computing and Computer-Assisted Intervention—MICCAI* (Lecture Notes in Computer Science), vol. 2488. Heidelberg, Germany: Springer, 2002, pp. 642–650.

[7] C. Tobon-Goméz, F. M. Sukno, C. Butakoff, M. Huguet, and A. F. Frangi, "Automatic training and reliability estimation for 3D ASM applied to cardiac MRI segmentation," *Phys. Med. Biol.*, vol. 57, no. 13, pp. 4155–4165, 2012.

[8] T. Heimann and H.-P. Meinzer, "Statistical shape models for 3D medical image segmentation: A review," *Med. Image Anal.*, vol. 13, no. 4, pp. 543–563, 2009.

[9] J. G. Bosch *et al.*, "Automatic segmentation of echocardiographic sequences by active appearance motion models," *IEEE Trans. Med. Imag.*, vol. 21, no. 11, pp. 1374–1383, Nov. 2002.

[10] S. C. Mitchell, J. G. Bosch, B. P. F. Lelieveldt, R. J. van der Geest, J. H. C. Reiber, and M. Sonka, "3-D active appearance models: Segmentation of cardiac MR and ultrasound images," *IEEE Trans. Med. Imag.*, vol. 21, no. 9, pp. 1167–1178, Sep. 2002.

[11] H. Zhang, A. Wahle, R. K. Johnson, T. D. Scholz, and M. Sonka, "4-D cardiac MR image analysis: Left and right ventricular morphology and function," *IEEE Trans. Med. Imag.*, vol. 29, no. 2, pp. 350–364, Feb. 2010.

[12] M. Wierzbicki, J. Moore, M. Drangova, and T. Peters, "Subject-specific models for image-guided cardiac surgery," *Phys. Med. Biol.*, vol. 53, no. 19, p. 5295, 2008.

[13] M. Sermesant, H. Delingette, and N. Ayache, "An electromechanical model of the heart for image analysis and simulation," *IEEE Trans. Med. Imag.*, vol. 25, no. 5, pp. 612–625, May 2006.

[14] M. Sermesant, C. Forest, X. Pennec, H. Delingette, and N. Ayache, "Deformable biomechanical models: Application to 4D cardiac image analysis," *Med. Image Anal.*, vol. 7, no. 4, pp. 475–488, 2003.

[15] M. Lynch, O. Ghita, and P. F. Whelan, "Segmentation of the left ventricle of the heart in 3-D+t MRI data using an optimized nonrigid temporal model," *IEEE Trans. Med. Imag.*, vol. 27, no. 2, pp. 195–203, Feb. 2008.
[16] K. Müller *et al.*, "Interventional heart wall motion analysis with cardiac C-arm CT systems," *Phys. Med. Biol.*, vol. 59, no. 9, pp. 2265–2284, 2014.
[17] C. Schwemmer, C. Rohkohl, G. Lauritsch, K. Müller, and J. Hornegger, "Residual motion compensation in ECG-gated interventional cardiac vasculature reconstruction," *Phys. Med. Biol.*, vol. 58, no. 11, pp. 3717–3737, 2013.
[18] E. Bergvall, E. Hedstrom, K. M. Bloch, H. Arheden, and G. Sparr, "Spline-based cardiac motion tracking using velocity-encoded magnetic resonance imaging," *IEEE Trans. Med. Imag.*, vol. 27, no. 8, pp. 1045–1053, Aug. 2008.
[19] K. Z. Abd-Elmoniem, M. Stuber, and J. L. Prince, "Direct three-dimensional myocardial strain tensor quantification and tracking using zHARP," *Med. Image Anal.*, vol. 12, no. 6, pp. 778–786, Dec. 2008.
[20] X. Papademetris, A. J. Sinusas, D. P. Dione, R. T. Constable, and J. S. Duncan, "Estimation of 3-D left ventricular deformation from medical images using biomechanical models," *IEEE Trans. Med. Imag.*, vol. 21, no. 7, pp. 786–800, Jul. 2002.
[21] L. Xia, M. Huo, Q. Wei, F. Liu, and S. Crozier, "Analysis of cardiac ventricular wall motion based on a three-dimensional electromechanical biventricular model," *Phys. Med. Biol.*, vol. 50, no. 8, pp. 1901–1917, 2005.
[22] H. Delingette *et al.*, "Personalization of cardiac motion and contractility from images using variational data assimilation," *IEEE Trans. Biomed. Eng.*, vol. 59, no. 1, pp. 20–24, Jan. 2012.
[23] H. Liu and P. Shi, "State-space analysis of cardiac motion with biomechanical constraints," *IEEE Trans. Image Process.*, vol. 16, no. 4, pp. 901–917, Apr. 2007.
[24] C. Ozturk, J. A. Derbyshire, and E. R. M. McVeigh, "Estimating motion from MRI data," *Proc. IEEE*, vol. 91, no. 10, pp. 1627–1648, Oct. 2003.
[25] G. Sundaramoorthi, A. Yezzi, and A. Mennucci, "Coarse-to-fine segmentation and tracking using sobolev active contours," *IEEE Trans. Pattern Anal. Mach. Intell.*, vol. 30, no. 5, pp. 851–864, May 2008.
[26] A. Yilmaz, X. Li, and M. Shan, "Contour-based object tracking with occlusion handling in video acquired using mobile cameras," *IEEE Trans. Pattern Anal. Mach. Intell.*, vol. 26, no. 11, pp. 1531–1536, Nov. 2004.
[27] N. Paragios and R. Deriche, "Geodesic active contours and level sets for the detection and tracking of moving objects," *IEEE Trans. Pattern Anal. Mach. Intell.*, vol. 22, no. 3, pp. 266–280, Mar. 2000.
[28] C. Xu and J. L. Prince, "Snakes, shapes, and gradient vector flow," *IEEE Trans. Image Process.*, vol. 7, no. 3, pp. 359–369, Mar. 1998.
[29] L. Zhuang, H. Liu, H. Bao, and P. Shi, "Volumetric meshfree framework for joint segmentation and motion tracking of the left ventricle," in *Proc. 4th IEEE Int. Symp. Biomed. Imag., Nano Macro*, Apr. 2007, pp. 396–399.
[30] D. Perperidis, R. H. Mohiaddin, and D. Rueckert, "Spatio-temporal free-form registration of cardiac MR image sequences," *Med. Image Anal.*, vol. 9, no. 5, pp. 441–456, 2005.
[31] K. McLeod, M. Sermesant, P. Beerbaum, and X. Pennec, "Spatio-temporal tensor decomposition of a polyaffine motion model for a better analysis of pathological left ventricular dynamics," *IEEE Trans. Med. Imag.*, vol. 34, no. 7, pp. 1562–1575, Jul. 2015.
[32] A. Bistoquet, J. Oshinski, and O. Škrinjar, "Myocardial deformation recovery from cine MRI using a nearly incompressible biventricular model," *Med. Image Anal.*, vol. 12, no. 1, pp. 69–85, 2008.
[33] R. Malladi, J. A. Sethian, and B. C. Vemuri, "Shape modeling with front propagation: A level set approach," *IEEE Trans. Pattern Anal. Mach. Intell.*, vol. 17, no. 2, pp. 158–175, Feb. 1995.
[34] P. M. Nielsen, I. J. L. LeGrice, B. H. Smaill, and P. J. Hunter, "Mathematical model of geometry and fibrous structure of the heart," *Amer. J. Physiol.*, vol. 260, no. 4, pp. H1365–H1378, 1991.
[35] M. Nash, "Mechanics and material properties of the heart using an anatomically accurate mathematical model," Ph.D. dissertation, Dept. Eng. Sci., School Eng., Univ. Auckland, Auckland, New Zealand, 1998.
[36] T. Belystchko, Y. Y. Lu, and L. Gu, "Element-free Galerkin methods," *Int. J. Numer. Methods Eng.*, vol. 37, no. 2, pp. 229–256, 1994.
[37] C. Kambhamettu and D. B. Goldgof, "Curvature-based approach to point correspondence recovery in conformal nonrigid motion," *CVGIP: Image Understand.*, vol. 60, no. 1, pp. 26–43, Jul. 1994.
[38] J. C. McEachen, A. Nehorai, and J. S. Duncan, "Multiframe temporal estimation of cardiac nonrigid motion," *IEEE Trans. Image Process.*, vol. 9, no. 4, pp. 651–665, Apr. 2000.
[39] O. Monga, N. Ayache, and P. Sander, "From voxel to curvature," in *Proc. IEEE Conf. Comput. Vis. Pattern Recognit.*, Jun. 1991, pp. 644–649.
[40] F. G. Meyer, R. T. Constable, A. J. Sinusas, and J. S. Duncan, "Tracking myocardial deformation using phase contrast MR velocity fields: A stochastic approach," *IEEE Trans. Med. Imag.*, vol. 15, no. 4, pp. 453–465, Aug. 1996.
[41] J. M. Guccione, A. D. McCulloch, and L. K. Waldman, "Passive material properties of intact ventricular myocardium determined from a cylindrical model," *J. Biomech. Eng.*, vol. 113, no. 1, pp. 42–55, 1991.
[42] M. Mellor and M. Brady, "Phase mutual information as a similarity measure for registration," *Med. Image Anal.*, vol. 9, no. 4, pp. 330–343, 2005.

HUAFENG LIU received the B.S. degree in optical engineering, the M.S. in measurement techniques and instruments, and the Ph.D. degree in positron emission tomography from the Department of Optical Engineering, Zhejiang University, in 1995, 1998, and 2001, respectively. From 2001 to 2003, he was a Post-Doctoral Fellow with The Hong Kong University of Science and Technology, where he was involved in statistical filtering and inverse mechanics strategies for cardiac image analysis and PET image reconstruction. He is currently a Full Professor with Zhejiang University. He is currently the Director of the ZJU-HAMAMATSU Joint Photonics Laboratory, which was co-founded by Hamamatsu Photonics K. K. and the Department of Optic-Electronic Information Engineering, Zhejiang University, in 1995, which focuses on biomedical imaging instrumentation, image reconstruction, and medical image analysis.

TING WANG received the B.S. degree in optical engineering from the Department of Optical Engineering, Zhejiang University in 2015. She is currently pursuing the Ph.D. degree with the Department of Optical Engineering, Zhejiang University. Her research interests are image reconstruction, medical image analysis, and radioluminescence microscopy.

LEI XU received the M.D. degree from Capital Medical University. He is currently an Associate Chief Physician and an Associate Professor with the Department of Radiology, Beijing Anzhen Hospital, Capital Medical University. His research interests and specialties are neuroimaging and cardiovascular imaging. He is currently a member of the Asian Society of Cardiovascular Imaging (ASCI) Information Committee, and a member of the ASCI-MRC.

PENGCHENG SHI received the Ph.D. degree in electrical engineering from Yale University in 1996. He has been a Professor and the Director of the Ph.D. Program with the B. Thomas Golisano College of Computing and Information Sciences, Rochester Institute of Technology, since 2007. His primary research interests are to develop and apply integrative system paradigms to biomedical imaging, image computing and intervention, and inverse physiology in the areas of personalized cardiac physiome, and dynamic, parametric, and multitracer PET imaging.